Rapid Joule Heating-Induced Structural Evolution of Nonstoichiometric Ordered Mesoporous Aluminum-Based Spinel Structures

Leyan Wang,[1] Qihang Chen,[1] Yong Quan Yeo,[1] Geok Leng Seah,[1] Hossein Akhoundzadeh,[2] Yee Yan Tay,[1] Teddy Salim,[1] Pio J. S. Buenconsejo,[1] Edward W. Corcoran Jr.,[3] Adam K. Usadi,[3] Jonathan M. McConnachie,[3] David T. Moore,[4] Rong Xu,[2] Zhong Chen,[1] and Kwan W. Tan[1,*]

Affiliations:

[1]School of Materials Science and Engineering, Nanyang Technological University, Singapore 639798, Singapore.

[2]School of School of Chemistry, Chemical Engineering and Biotechnology, Nanyang Technological University, Singapore 637459, Singapore.

[3]ExxonMobil Technology and Engineering Company, Annandale, New Jersey 08801, United States.

[4]Materials Chemistry & Computation Sciences, National Renewable Energy Laboratory, Golden, Colorado 80401, United States.

*Correspondence: kwtan@ntu.edu.sg

Abstract

Coupling self-assembly with ultrashort transient heating at high temperatures effectively accelerates reaction kinetics through enhanced transformation pathways. This approach provides precise control over crystalline phase characteristics and enables emergent collective properties and functionalities in mesoporous inorganic materials. Here, we describe the structural evolution and rapid formation of highly crystalline, well-ordered mesoporous magnesium aluminate defect spinel structures with nonstoichiometric compositions, achieved in seconds via block copolymer-directed self-assembly and Joule heating. Isothermal experiments conducted ex situ demonstrated Joule heating-induced acceleration of the amorphous-to-spinel transition. The process aligned with the Johnson-Mehl-Kolmogorov-Avrami model, revealing an instantaneous surface nucleation and diffusion-controlled growth mechanism requiring significantly lower activation energy compared to conventional thermal treatments. Further exploration of the ultrafast approach led to the development of an ordered mesoporous defect spinel-carbon framework decorated with in situ crystallized platinum nanoparticles. This composite structure exhibited enhanced thermal and mechanical stability under high temperature reducing environments, demonstrating its potential for thermal catalytic applications. Understanding Joule heating-induced crystallization kinetics and phase transformations on transient timescales may reveal novel crystalline phases and functionalities inaccessible through conventional heating of nonstoichiometric compositions.

1. Introduction

Highly crystalline, well-ordered aluminum-based oxides with large specific surface areas, regular pore structures, and periodic architectures have garnered significant scientific and industrial interests for various applications such as adsorption, separation and catalysis.[1–8] Incorporating metals such as copper (Cu), cobalt (Co), magnesium (Mg) and nickel into ordered mesoporous alumina (Al_2O_3) enhances its functionality by improving surface and structural properties, introducing new acidic/basic active sites, and providing greater thermal stability, mechanical strength and chemical inertness.[9–17]

Bottom up self-assembly utilizing surfactants and block copolymers (BCPs) to direct organic/inorganic additives offers a straightforward method for creating well-ordered hybrid mesostructures.[18–28] Niesz et al.[2] and Yuan et al.[3] demonstrated a one-pot approach where Pluronic tri-BCPs (F127, P123) were mixed with aluminum alkoxide precursors and acid catalysts under controlled hydrolysis. This method, followed by solvent evaporation-induced self-assembly (EISA) and furnace annealing, yielded well-defined mesoporous Al_2O_3 hexagonal cylinders. Recently, we improved the protocol by first preparing a stable Al_2O_3 sol-derived additive.[5,6] When combined with F127, the stabilized additive enabled a broader range of well-ordered mesoporous structures through EISA and heat treatment, including lamellar, hexagonal cylinders, body-centered cubic lattices, and hierarchically ordered Al_2O_3 with interconnected networks of macropores and hexagonally arranged mesopores.[6]

Ordered mesoporous metal aluminate spinel structures, which offer higher specific surface areas, mesoporosity, and enhanced mechanical, thermal and chemical stability, compared to mesoporous γ-Al_2O_3, are highly sought after for industrial refining, hydrogenation and catalysis reactions.[14,16,29,30] Jaroniec and co-workers performed a series of one-pot synthesis experiments using Pluronic P123, Al alkoxide/nitrate/boehmite precursors, and various dopant metal salts

through EISA and calcination, resulting in ordered hexagonal cylinders and disordered wormlike mesoporous Al_2O_3-supported mixed metal oxides doped with ~10% of Co, Cu, Mg, and Ni.[9,10,13] Upon furnace annealing above 600 °C, these mixtures transformed into metal aluminate spinel ($MeAl_2O_4$, Me = Co, Cu, Mg, Ni) supported on mesoporous γ-Al_2O_3.[9,13] Similarly, Li et al. employed a one-pot method to synthesize P123-directed Mg-Al-O composites with varying Mg/Al compositions.[11] Small-angle X-ray scattering (SAXS) and transmission electron microscopy (TEM) data revealed that only composites with Mg loadings below 30% retained their periodic mesostructure after calcination at 900 °C. Additionally, wide-angle X-ray scattering (WAXS) data confirmed the presence of $MgAl_2O_4$-spinel reflections alongside the dominant γ-Al_2O_3 phase.

Yoon et al. fabricated Ni nanoparticles on P123-directed mesoporous Mg-Al-O structures through a three-cycle annealing process at 800 °C for 10 hours.[14] The first heating cycle removed P123 BCP, forming mesoporous Mg-Al-O structures. Ni nitrate was then impregnated, followed by a second heating cycle to incorporate Ni into atomic vacancies. The final hydrogen annealing cycle transformed the material into Ni-decorated mesoporous Mg-Al-O defect spinel structures, though this also resulted in a disordered morphology and reduced surface area.[14] Alvar and Rezaei also incorporated Ni nanoparticles into disordered mesoporous $MgAl_2O_4$ spinel with pores smaller than 4 nm, using cetyltrimethylammonium bromide as a structure-directing surfactant.[17] Pan et al. synthesized ordered F127-directed Mg-Al-O composites with ~11% Mg content, where TEM and WAXS showed precipitated nanoparticles within crystalline γ-Al_2O_3 mesopore channels after calcination at 1000 °C, without transformation to the spinel phase.[12] In another study, Ganesh et al. used microwave irradiation on Al hydroxide and magnesium oxide (MgO) precursors for 60 min, forming agglomerated powders of MgO, α-Al_2O_3 and $MgAl_2O_4$-spinel with large crystallite sizes of ~60–70 nm.[31]

The transformation from an amorphous state to spinel in Mg-Al-O systems requires high temperatures and is influenced by factors such as stoichiometric composition, counter-diffusion of Al^{3+} and Mg^{2+} cations, oxygen diffusion, structural defects, and chemical reactions.[13,16] However, furnace annealing at high temperatures for extended periods often leads to excessive crystallite growth and agglomeration, causing mesostructural collapse and textural degradation.[5,6,14,20,32] To address these challenges, we developed a Joule heating-based method known as self-assembly and nonequilibrium annealing phase transformation (SNAP). This technique enables the rapid generation of freestanding, bulk monoliths of highly crystalline, long-range ordered mesoporous oxides and carbon structures within seconds, including γ-Al_2O_3, α-Fe_2O_3, anatase TiO_2, and graphitic carbon.[33] To the best of our knowledge, the structural evolution induced by Joule heating in crystalline ordered mesoporous inorganic systems and various other nanomaterial combinations remains largely elusive.[34,35] Moreover, ultrafast Joule heating which enables rapid thermal activation followed by quenching, may allow access to high-energy, metastable states that result in materials with unconventional phases and unique structural features.[36–40]

In this study, we report the structural evolution of highly crystalline, periodically ordered mesoporous γ-Al_2O_3 and magnesium aluminate ($Mg_xAl_yO_4$) defect spinel structures during Joule heating, occurring within seconds. The ultrashort heating process facilitated the transformation of nonstoichiometric, ordered mesoporous F127-Al_2O_3-Mg hybrid composites into fully crystalline defect spinel structure; a phenomenon not previously observed in self-assembled mesoporous composites. Quantitative X-ray scattering analysis of Al_2O_3-carbon and $Mg_xAl_yO_4$-carbon composites during ex situ isothermal crystallization, interpreted using the Johnson-Mehl-Kolmogorov-Avrami (JMKA) model, revealed instantaneous surface nucleation and diffusion-controlled growth with significantly reduced activation energies. Finally, we demonstrated the one-pot synthesis of well-dispersed Pt nanoparticles on the pore walls of mesoporous $Mg_xAl_yO_4$

spinel-carbon composites, which maintained high thermal and structural integrity during methylcyclohexane dehydrogenation at 350 °C for 16 hours.

2. Experimental Section

Materials. All chemicals were used as received. Pluronic F127 (PEO-*b*-PPO-*b*-PEO, 12.6 kg/mol), aluminum tri-*sec*-butoxide (Al-(O^sBu)$_3$), 97%), magnesium nitrate hexahydrate ($Mg(NO_3)_2 \cdot 6H_2O$), (1,5-cyclooctadiene) dimethyl platinum(II) ($Pt(cod)(Me)_2$, 97%), were obtained from Sigma-Aldrich. Absolute ethanol (EtOH, 200 proof) was obtained from Merck. Nitric acid (HNO_3, 69 wt % in water) was obtained from Honeywell International.

Synthesis of F127-Al_2O_3 Hybrid Monoliths. The F127-Al_2O_3 hybrid monoliths were prepared as reported elsewhere.[6] Briefly, an Al_2O_3-sol-additive mother solution was obtained by mixing 3.76 g (81.7 mmol) of EtOH, 1 g (4.0 mmol) of Al(O^sBu)$_3$ and 0.421 mL (6.5 mmol) of HNO_3 sequentially and then stirred for >12 h under ambient conditions. Subsequently, a 1.53 g (18.7 wt% Al(O^sBu)$_3$) aliquot of the sol additive was added to a 1.80 g F127 solution (10 wt% in EtOH) and stirred for 30 min. The resulting colorless transparent solutions were cast in 5 mL Teflon beakers set on a glass Petri dish covered with hemispherical glass dome and heated at 50 °C for EISA over 3-5 days. The hybrid monoliths were then thermally aged at 130 °C in a vacuum oven overnight.

Synthesis of F127-Al_2O_3-Mg Hybrid Monoliths. The F127-Al_2O_3-Mg hybrid monoliths were prepared as reported elsewhere.[33] An additive sol mother solution of 90:10 Al/Mg molar ratio was prepared by first mixing 3.76 g (81.7 mmol) of EtOH, 0.9 g (3.6 mmol) Al(O^sBu) and 0.368 mL (5.7 mmol) HNO_3 sequentially and stirred for >12 h, followed by the addition of 0.12 g (0.4 mmol) of $Mg(NO_3)_2$ $6H_2O$ and stirring for another 30 min to dissolve the Mg salt. A 1.53 g aliquot of the resultant Al_2O_3-Mg sol solution was added to a 1.80 g of F127 solution (10 wt% in EtOH) and stirred for 30 min. This was followed by EISA and thermal ageing as described above. Other F127-Al_2O_3-Mg hybrid samples with Al/Mg molar ratios of 80:20, 70:30, and 50:50 were

prepared with their respective additive sol mother solutions. It is noted that in the preparation of all sol mother solutions, the added inorganic Al and Mg sol precursors were maintained at the same concentration of 4.0 mmol

Synthesis of Pt@F127-Al_2O_3-Mg Hybrid Monoliths. An additive sol mother solution of 90:10 Al/Mg molar ratio was first prepared as described above, followed by the addition of $Pt(cod)(Me)_2$ and stirring for another 10 min to dissolve the Pt salt. Appropriate aliquots were added into the F127 solution (10 wt% in EtOH) to prepare the hybrid samples by EISA and thermal ageing as described above. A 5 wt % Pt-loaded composite is composed of 1 g (4.0 mmol) $Al(O^sBu)_3$, 0.116 g (0.451 mmol) $Mg(NO_3)_2 \cdot 6H_2O$ and 0.020 g (0.061 mmol) $Pt(cod)(Me)_2$. A 1 wt % Pt-loaded composite is composed of 1 g (4.0 mmol) $Al(O^sBu)_3$, 0.116 g (0.451 mmol) $Mg(NO_3)_2 \cdot 6H_2O$ and 0.004 g (0.012 mmol) $Pt(cod)(Me)_2$.

Thermopolymerization of Hybrid Composite Monoliths. The hybrid composites were heated in a tube furnace at 400 °C (2 h) with a ramp rate of 1 °C/ min under inert nitrogen/argon to thermopolymerize the F127 BCP into resin.

Joule Heating of Hybrid Composite Monoliths. The Joule heating experiments were conducted as described elsewhere.[33] Briefly, a monolithic hybrid sample was sandwiched between a carbon felt and electrically heated by a DC power source under mild vacuum. The samples were heated at temperatures of 1000 to 1200 °C with annealing dwells between 1 to 100 s.

Furnace Heat Treatment. For control experiments, selected composite samples were heated in a tube furnace under static air from 450 to 900 °C (3 h), with a ramp rate of 1 °C/min, to remove the copolymer and facilitate the crystallization of inorganic components.

Methylcyclohexane Dehydrogenation Reaction Experiments. The dehydrogenation of methylcyclohexane reaction was conducted in an atmospheric fixed-bed continuous flow system using a quartz reactor (internal diameter of 6.3 mm). The mesoporous 1wt%-Pt@$Mg_xAl_yO_4$ sample (90 mg) was diluted with sand (1.5 g) and placed among two parts of sand. Before the dehydrogenation reaction, the sample was reduced at 380 ºC for 2 h in hydrogen with a flow rate of 40 mL/min. The temperature of the reactor was decreased to 350 °C and held for a total of 1000 min. The reaction was initiated by injecting methylcyclohexane with the nitrogen carrier gas at flow rates of 0.016 and 5.1 mL/min, respectively, into the reactor. An online gas chromatograph (GC) with a flame ionization detector (FID) and a thermal conductivity detector (TCD) were used for the analysis of the products in the gas phase.

Characterization. SAXS and WAXS measurements were collected with a Xenocs NanoinXider using Cu K_α radiation source and Dectris Pilatus 3 detectors. The 2D SAXS/WAXS patterns were azimuthally integrated around the beam center into 1D scattering intensity curves plotted against the scattering vector magnitude $q = 4\pi sin\theta/\lambda$, where θ is half of the total scattering angle and λ is the X-ray wavelength. The cylinder-to-cylinder distance of *p*6*mm* lattice was calculated using $d = 4\pi/\left(\sqrt{3}q^*\right)$, where q^* is the scattering vector of the principal peak. Structural analysis of WAXS data was performed using TOPAS (version 6) by fitting the WAXS patterns with the $Mg_{0.388}Al_{2.408}O_4$ defect spinel (PDF 00-048-0528) and γ-Al_2O_3 (PDF 00-010-0425) structures.[41,42]

TEM and selected area electron diffraction (SAED) measurements were obtained using a JEOL-2100F electron microscope operating at an accelerating voltage of 200 kV equipped with the Gatan Ultrascan 1000XP CCD camera. Scanning transmission electron microscopy (STEM) using high annular dark field (HAADF) imaging mode and energy dispersive spectroscopy (EDS) was conducted with a JEOL JEM-ARM200F aberration-corrected electron microscope. The instrument is equipped with a probe corrector operating at an accelerating voltage of 200 kV, a

Gatan 4K × 4K One-View CMOS camera, an Oxford X-Max TLE 100 mm^2 windowless silicon drift detector, and high-angle annular STEM detectors.

Nitrogen sorption measurements were conducted using the Micromeritics ASAP 2020 and Tristar II 3020 at −196 °C. All samples were degassed at 130 °C overnight under vacuum/nitrogen before measurements. The specific surface areas were obtained using the Brunauer–Emmett–Teller (BET) method below 0.2 P/P_0.[43] The mesopore size distributions were obtained using the Barret-Joyner-Halenda (BJH) method, along with the Kruk-Jaroniec-Sayari (KJS) model correction, by analyzing the adsorption branch of nitrogen isotherms.[44,45] Single-point adsorption pore volumes were extracted at 0.99 P/P_0.

X-ray photoelectron spectroscopy (XPS) analysis was performed using an AXIS Supra spectrometer (Kratos Analytical, UK) equipped with a hemispherical analyzer and a monochromatic Al Kα source (1487 eV) operating at 15 mA and 15 kV. The XPS spectra were acquired from an analysis area of 700 × 300 μm^2 at a take-off angle of 90 °. A pass energy of 160 and 20 eV was used for survey and high-resolution scans, respectively. A 3.1 V bias was applied to prevent charge build-up on the composite samples. The XPS samples were prepared by pressing the powdered particles on carbon tape.

3. Results and Discussion

3.1 Synthesis of Ordered Al_2O_3-Mg Mesostructures.

The one-pot BCP self-assembly-directed synthesis approach is highly versatile, enabling the formation of multifunctional and well-ordered materials combinations. Figure 1 illustrates the schematic procedure of the SNAP method used to form highly crystalline and well-ordered mesoporous γ-Al_2O_3, $Mg_xAl_yO_4$-spinel and Pt@$Mg_xAl_yO_4$. As an example, to fabricate Pt@$Mg_xAl_yO_4$, we first prepared the inorganic additives in a separate vial by sequentially mixing

the Al alkoxide, nitric acid catalyst, Mg salt and Pt salt in ethanol to form a stable sol solution precursor.[6] Appropriate amounts of these inorganic additives were then added into the structure-directing F127 tri-BCP ethanolic solution to form hybrid micelles. The micelle core is comprised of hydrophobic PPO domains that selectively attract Pt salt, while the corona consists of hydrophilic PEO domains and is hydrogen-bonded to Al_2O_3-Mg sol precursors.[6,46] Monoliths of well-defined, hexagonally arranged mesoporous inorganic structures with high crystallinity were obtained after undergoing the EISA process, BCP thermopolymerization, and Joule heating for short durations of 1 to 100 s at temperatures ranging from 1000 to 1200 °C.[33] Herein, the samples are denoted as Al_2O_3-Mg-*X*, where *X* represents the molar percentage of Mg relative to Al, ranging from 10 to 50.

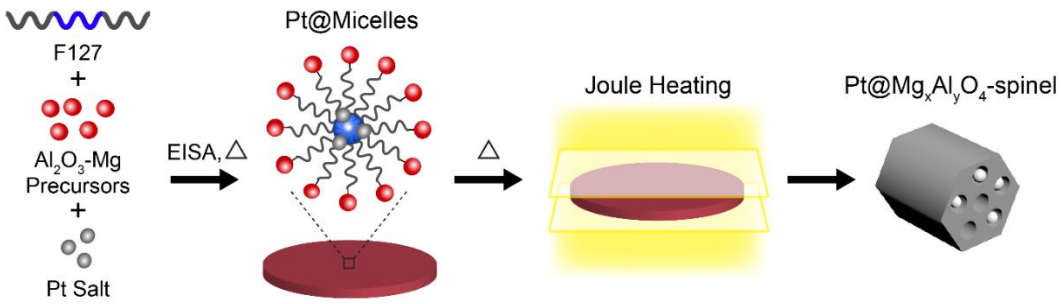

Figure 1. Schematic for SNAP-derived well-ordered mesoporous Pt@$Mg_xAl_yO_4$ structures.

3.2 Crystallite Size Evolution of SNAP-Derived Mesoporous γ-Al_2O_3.

The SNAP method enables rapid crystallization of mesoporous Al_2O_3 hexagonal cylinders from the amorphous state to the γ-phase within short annealing dwells in less than 5 seconds at high temperatures.[33] To understand the crystalline structural evolution of ordered γ-Al_2O_3, we performed isothermal Joule heating treatments of the monolithic hybrid samples at three different temperatures, i.e., 1000, 1090, and 1155 °C, for annealing dwells of 1 to 100 s.

Figure 2a and b shows the SAXS and WAXS patterns of ordered mesoporous γ-Al_2O_3 structures after Joule heating at 1000 °C. Firstly, SAXS data in Figure 2a confirmed that all mesoporous γ-Al_2O_3 samples retained the *p*6*mm* lattice order for all annealing dwells at 1000 °C. Secondly, an annealing dwell of 1 s was insufficient to crystallize the sample, as indicated by the absence of WAXS reflections (Figure 2b). The characteristic peaks of the γ-Al_2O_3 phase first appeared with a longer annealing dwell of 10 s, as shown by the two most intense peaks at 2θ of 37.6 and 46.3°, corresponding to the (311) and (400) planes, respectively. As the annealing dwells further increased from 20 to 100 s, the two main peaks gained intensity and narrowed, indicating the enlargement of crystallite sizes and the emergence of other secondary reflections. The misalignment of the WAXS peaks from the expected (400) plane position is attributed to residual stress induced by rapid heating and cooling cycles during Joule heating. Similar trends were observed in the SAXS and WAXS data of other samples annealed at higher temperatures of 1090 and 1155 °C for different annealing dwells up to 103 s, with all mesoporous crystalline γ-Al_2O_3 samples retaining their *p*6*mm* mesoscale periodic order (see Figure S1).

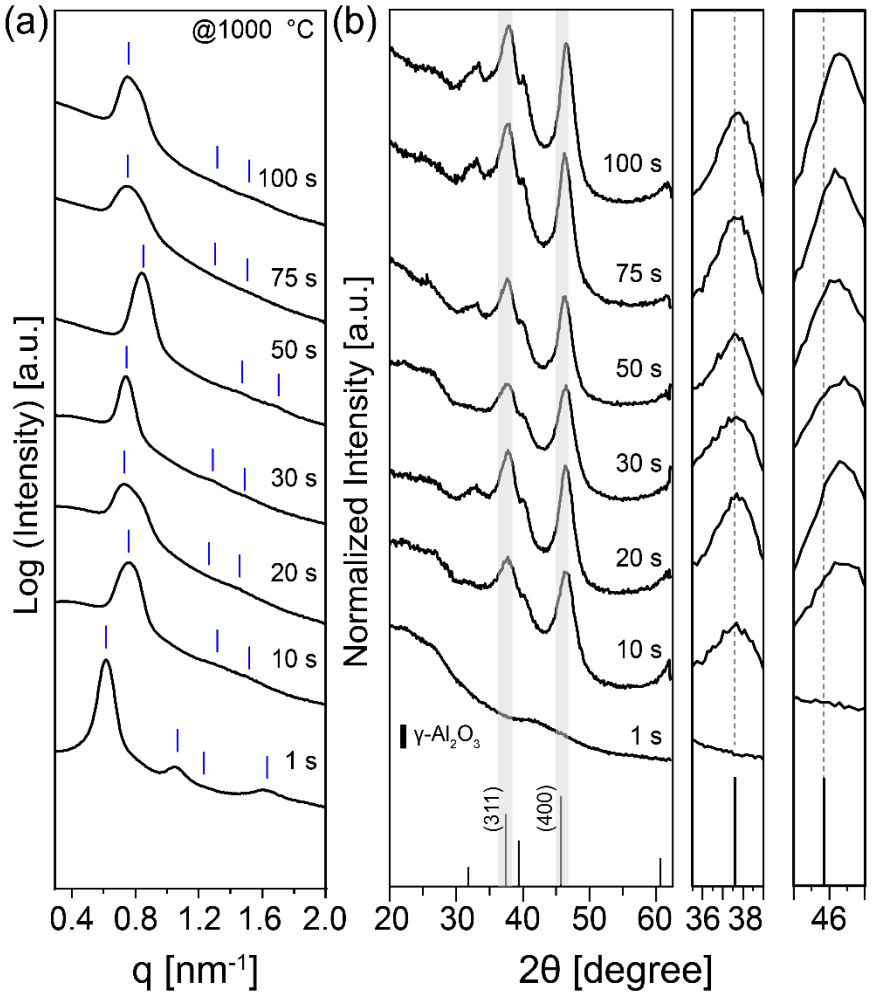

Figure 2. (a) SAXS and (b) WAXS patterns of mesoporous γ-Al_2O_3 samples after Joule heating at 1000 °C for different durations as indicated. Tick marks (blue) for the expected reflections of the *p*6*mm* symmetry are shown in (a). WAXS peak markings and relative intensities (black) for γ-Al_2O_3 (PDF- 00-010-0425) are shown in (b). The two panels on the right hand side show the WAXS reflections at angular positions of 36 to 39° and 45 to 47°, respectively. The dashed lines are added into the panels to guide the eye.

3.3 Isothermal Kinetic Modeling of SNAP-Derived γ-Al_2O_3 Crystallization.

Kinetic analysis in literature typically tracks a material's specific property, such as crystallinity percentage or mass changes, under isothermal or isochronal conditions to pinpoint the onset and end of solid-state transformation.[47,48] We monitored the evolution of the γ-Al_2O_3 crystallite size (*D*) as a direct indicator of amorphous-to-crystalline transformation and crystallite growth under isothermal Joule heating conditions. We estimated the apparent crystallite size with respect to the most prominent WAXS reflections at ~38 and 46° using the Scherrer equation. Figure 3a shows the γ-Al_2O_3 crystallite size increasing with Joule heating temperatures and times. Crystallite growth was the fastest within the first 20 s, then slowed, reaching plateaus around 60 s. Notably, the respective γ-Al_2O_3 samples at the plateaus, with the largest crystallite sizes, maintained their mesoscale periodic order even after extended durations of Joule heating.

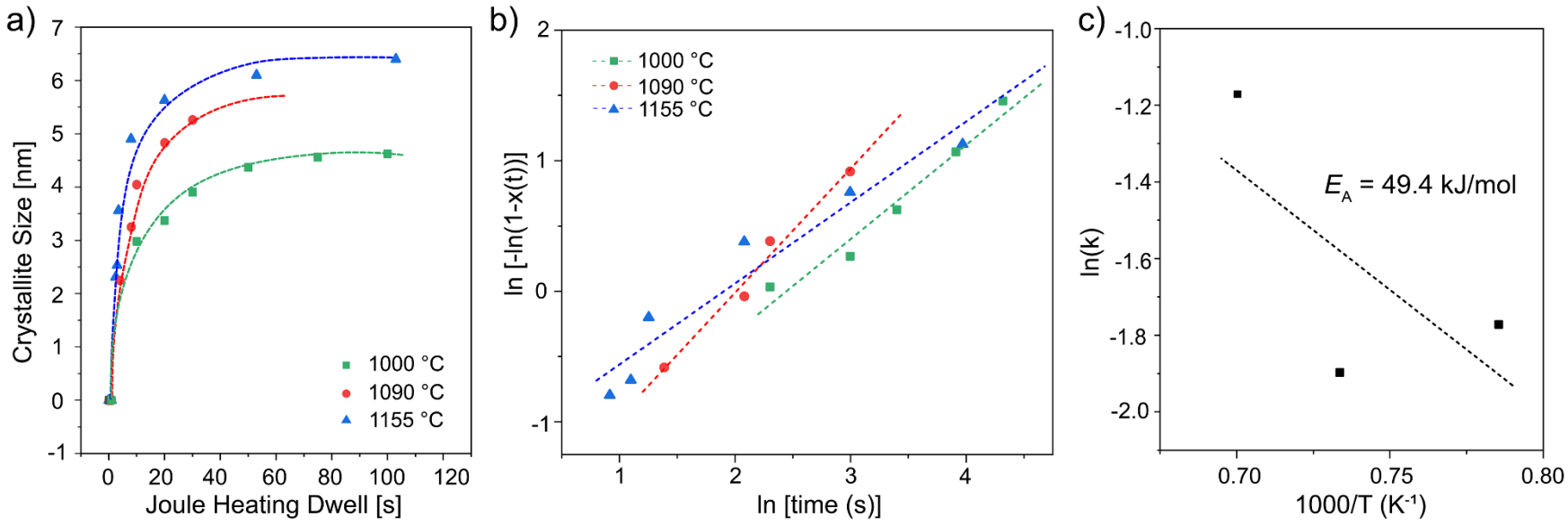

Figure 3 (a) Line plots tracking the growth of γ-Al_2O_3 crystallites across various Joule heating temperatures and annealing times, as indicated, with dashed lines added to guide the eye. (b) Linearized JMKA model plots and (c) Arrhenius graph illustrating isothermal Joule heating-induced crystallization of ordered mesoporous γ-Al_2O_3 samples at various temperatures, as indicated. The dashed lines were obtained from linear regression analysis of the respective data points.

The Johnson-Mehl-Kolmogorov-Avrami (JMKA) model (eq. 1), which is also commonly expressed in a linearized form (eq. 2), is a well-established model to describe phase transformation kinetics and crystallization mechanism under isothermal conditions:[49–51]

$$x(t) = 1 - \exp\left(-Kt^n\right) \quad (1)$$

$$\ln\{-\ln[1 - x(t)]\} = \ln K + n \ln t \quad (2)$$

where *x(t)* describes the degree of transformation over time, *K* is the time-independent rate constant, and *n* represents the Avrami exponent, a pure number indicating the dimensionality of the transformation and independent of temperature.[49–51] The degree of transformation, or fraction of crystallinity *x*(*t*), is calculated using eq. 3. Initially, the crystallite size for the amorphous sample at time point 0 s is set as *x*(0) = 0. Upon reaching the largest crystallite size whilst retaining mesoscale structure order, x(t_{end}) is equal to 1 (see respective plateaus in Figure 3a).

$$x(t) = \frac{D(t)}{D(t_{end})} \quad (3)$$

The temperature-dependent rate constant *K* can be assumed to take the form of the Arrhenius equation[47] as:

$$K = A \exp\left(-\frac{E_a}{RT}\right) \quad (4)$$

$$ln(K) = -\frac{E_a}{RT} + \ln(A) \quad (5)$$

where *A* is a constant, E_a is the activation energy, *T* is the Joule heating temperature and *R* is the gas constant, 8.314 J mol^{-1} K^{-1}.

Figure 3b presents the linearized plots of $\ln\{-\ln[1-x(t)]\}$ versus $\ln t$ for the isothermal γ-Al_2O_3 samples subjected to Joule heating at 1000, 1090, and 1155 °C, which aligned excellently with the JMKA model. The correlation coefficients (R^2) for these fits ranged from 0.93 to 0.98 as detailed in Table 1. The Avrami exponent *n* and rate constant *K* values for these Joule heating temperatures ranged from 0.62 to 0.95 and 0.17 to 0.31 s^{-1}, respectively. In addition, the linearized Arrhenius plot in Figure 3c yielded an activation energy E_a of 49.4 kJ mol^{-1}.

We observed several notable phenomena. First, the Avrami exponents *n* ranging from 0.62 to 0.95 indicated that rapid Joule heating likely facilitates instantaneous nucleation, followed by accelerated crystallite growth.[52,53] In particular, γ-Al_2O_3 crystallite growth exhibited characteristics of both interface- and diffusion-controlled mechanisms,[51] attributed to complex atomic diffusion behaviors triggered by a rapid increase to high temperatures, brief holding dwell times, and subsequent rapid quenching. To further elucidate the transformation kinetics under these transient isothermal annealing conditions, we performed a global fit of the JMKA model to all collected data, as illustrated in Figure S2a. The analysis yielded the global Avrami exponent *n* and rate constant *K* parameters of 0.60 and 0.30 s^{-1}, respectively, suggesting that Joule heating predominantly favors diffusion-controlled crystallite growth.

Secondly, the activation energy required to transform "bulk" mesoporous Al_2O_3 monoliths from an amorphous state to the γ-phase via Joule heating was significantly lower than that for conventional furnace-heated Al_2O_3 thin films (~49.4 versus 443.9 kJ/mol).[54] The difference in activation energy could be attributed to Joule heating, which offers a more efficient pathway for solid-state phase transformations, thereby facilitating enhanced atomic diffusion mobility and accelerating reaction kinetics. Previous studies by Banfield et al. and Tolbert et al. have shown that crystallization of nanocrystalline titania at elevated temperatures is primarily driven by surface nucleation.[47,55,56] It is reasonable to assume that Joule heating-induced crystallization of

bulk mesoporous γ-Al_2O_3 monoliths occurred through instantaneous surface nucleation followed by diffusion-controlled growth, preferentially along the hexagonal mesopore walls.[47,52]

Table 1. Summary of Joule heating-induced crystallization of crystalline ordered mesoporous Al-based oxide systems.

sample	temperature (°C)	n^a	K (s^{-1})	R^2	$E_a{}^b$ (kJ mol^{-1})
γ-Al_2O_3	1000	0.72	0.17	0.96	49.4
	1090	0.95	0.15	0.98	
	1155	0.62	0.31	0.93	
Al_2O_3-Mg-10	1000	0.63	0.27	0.99	34.7
defect spinel	1090	0.73	0.19	0.98	
	1155	0.63	0.42	0.99	

[a]Derived from the JMKA model (eq. 1). [b]Derived from the Arrhenius equation (eq. 4).

3.4 Influence of Mg Composition on F127-Al_2O_3-Mg Morphologies.

The addition of dopant metals (Me) introduces new functionalities and enhances specific properties of mesoporous Al_2O_3 structures. Jaroniec et al. have elaborated on two key factors in the formation of disordered mesoporous spinel structures with large pores: the chemical reaction (eq. 6) and the counter-diffusion of cations – divalent Me^{2+} and trivalent Al^{3+}.[13] Specifically, the rates at which Me^{2+} and Al^{3+} cations move in opposite directions toward their respective metal oxide interfaces, forming the $MeAl_2O_4$ spinel structure, depend on the reaction energy barrier, temperature, structural defect population, and the diffusion of oxygen and vacancies.[13]

$$Al_2O_3 + MeO \rightarrow MeAl_2O_4 \qquad (6)$$

Figure S3 presents the SAXS and WAXS data of F127-Al_2O_3-Mg hybrid composites with varying Mg loadings (5 to 50%), along with the corresponding mesoporous Al_2O_3-Mg structures after calcination at 450 °C. The SAXS patterns of hybrid samples with lower Mg contents in Figure S3a (Al_2O_3-Mg-5 and Al_2O_3-Mg-10) exhibited highly intense primary peaks and several higher order secondary reflections at angular positions of $(q/q^*)^2$ = 1, 3, 4, 7, consistent with the hexagonal *p6mm* lattice and long-range order. As the Mg composition increased to 30% (Al_2O_3-Mg-20 and Al_2O_3-Mg-30), the reduced intensities of the principal peaks, along with absence of secondary reflections, indicated the loss of long-range order with varying extent. At the highest Mg composition (Al_2O_3-Mg-50), the broad SAXS curve of low intensity indicated a disordered morphology. The addition of Mg salt as a coprecursor to the Al_2O_3 sol additive likely introduced new complexities in the interactions between the organic structure-directing F127 copolymer and inorganic additives.[27,57] This could have caused disruptions to the self-assembly process and hindered the ordering of mesoscale structures.

The SAXS spectra of mesoporous inorganic counterparts after furnace calcination at 450 °C, shown in Figure S3b, present a similar trend. Mesoporous Al_2O_3-Mg samples with lower Mg contents (Al_2O_3-Mg-5 and Al_2O_3-Mg-10) retained the *p6mm* lattice with long range order, as corroborated by the multiple SAXS reflections with strong intensities. However, the SAXS patterns of higher Mg loading samples (Al_2O_3-Mg-20 and Al_2O_3-Mg-30) retained the peaks consistent with the *p6mm* symmetry but with lower intensities. The WAXS patterns, featuring broad humps in the absence of obvious diffraction peaks as shown in Figure S3c, denote that all the ordered mesoporous Al_2O_3-Mg materials were amorphous. In contrast, the prominent peak at 2θ = 43.6° in the WAXS pattern of the disordered Al_2O_3-Mg-50 sample suggested phase separation, indicative of the selective crystallization of some large MgO grain areas.

We further subjected the ordered mesoporous Al_2O_3-Mg-10 to furnace annealing at higher temperatures ranging from 600 to 900 °C for 3 h. The SAXS patterns shown in Figure S4a

revealed that all Al_2O_3-Mg-10 samples retained long range ordered *p6mm* symmetry up to 800 °C (sample (i) to (iii)). WAXS data in Figure S4b indicated the crystallization onset temperature was delayed to 800 °C, likely due to the inhibitory effects of the Mg dopant. For the Al_2O_3-Mg-10 sample annealed at 800 °C (sample (iii)), we observed a stronger reflection intensity at 2θ = 37.6° compared to 45.7°, opposite to the γ-Al_2O_3 phase trend. Furthermore, a new broad reflection at 2θ = 56.5° suggested the emergence of a new phase, likely the (422) plane of the $Mg_xAl_yO_4$ defect spinel structure. However, the broadness and low intensity of these new reflections indicated the $Mg_xAl_yO_4$ defect spinel was a minority phase supported on the dominant crystalline γ-Al_2O_3 structure. At 900 °C, the SAXS pattern for Al_2O_3-Mg-10 (sample (iv)) exhibited a broad peak with low intensity, and the TEM micrograph in Figure S4(c), indicated a significant loss of long range mesostructure order. It is likely that the uncontrolled enlargement of crystallites at 900 °C resulted in partial mesostructural collapse (see HR-TEM image in Figure S4d). The estimated crystallite size from Scherrer analysis was ~10.8 nm.

3.5 Structural Evolution and Isothermal Kinetics of SNAP-Derived Ordered Mesoporous $Al_xMg_yO_4$-Defect Spinel Structures.

We applied Joule heating on the ordered Al_2O_3-Mg-10 hybrid composites to investigate their phase transformation behaviors at the atomic and nanoscale levels. Figures 4 and S5 display the SAXS and WAXS data of ordered Al_2O_3-Mg-10 samples after isothermal Joule heating at temperatures of 1000, 1090 and 1155 °C for annealing dwells ranging from 1 to 100 s. The SAXS patterns in Figures 4a, S5a, and S5c indicated that the ordered *p6mm* morphology of all Al_2O_3-Mg-10 samples was retained after Joule heating, despite some decrease in the intensities of principal peaks. All Al_2O_3-Mg-10 samples underwent crystallization induced by Joule heating within the first 20 seconds of annealing (Figures 4b, S5b, and S5d). Additionally, the intensity of the secondary peak at $2\theta \approx 57°$ became stronger and more resolved with higher temperatures

and longer dwells. This reflection matches well with the (422) plane of the reference nonstoichiometric $Mg_{0.388}Al_{2.408}O_4$ defect spinel structure (PDF 00-048-0528).

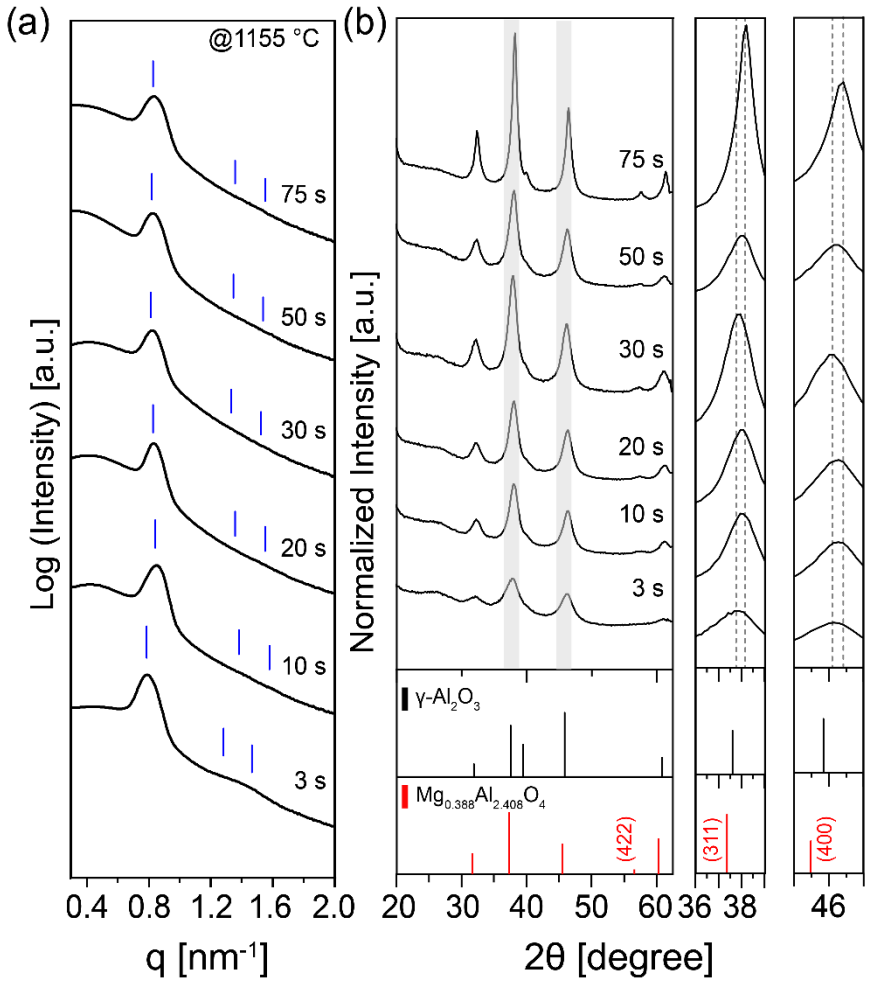

Figure 4. (a) SAXS and (b) WAXS patterns of mesoporous Al_2O_3-Mg-10 samples after Joule heating at 1155 °C for different durations as indicated. Tick marks (blue) for the expected reflections of the *p*6*mm* symmetry are shown in (a). WAXS peak markings and relative intensities for γ-Al_2O_3 (black, PDF 00-010-0425) and $Mg_{0.388}Al_{2.408}O_4$ defect spinel (red, PDF 00-048-0528) are shown in (b). The two panels on the right hand side show the WAXS reflections at angular positions of 36 to 39° and 45 to 47°, respectively. The dashed lines are added into the panels to guide the eye.

Moreover, the intensity of the reflection at 2θ around 38° was the highest among all other reflections, followed by the peak around 46°. This difference in relative peak intensity is consistent with that of the reference $Mg_{0.388}Al_{2.408}O_4$ defect spinel structure and contrasts with the γ-Al_2O_3 phase (PDF 00-010-0425), where the most intense reflection was observed around 46°. These observations provide additional evidence of the structural transformation into the $Mg_xAl_yO_4$ defect spinel structure, with reflections around 38° and 46° corresponding to the (311) and (400) planes, respectively.

γ-Al_2O_3 is considered to have a metastable cubic defect spinel-type structure (space group $Fd\bar{3}m$) with O atoms in a cubic close packed arrangement and Al atoms occupying both tetrahedral and octahedral sites.[1,13,58] The nonstoichiometric addition of Mg into γ-Al_2O_3 promotes the formation of a more thermodynamically stable $Mg_xAl_yO_4$ defect spinel structure (space group $Fd\bar{3}m$, PDF 00-048-0528), with larger Mg atoms preferentially occupying the tetrahedral sites and smaller Al atoms in the octahedral positions, resulting in a larger lattice constant.[16,59] Conventional furnace heating typically results in the $Mg_xAl_yO_4$ as a minority phase supported on γ-Al_2O_3.[9,13] In contrast, rapid Joule heating can promote the transformation into a complete nonstoichiometric $Mg_xAl_yO_4$ defect spinel.

We examined the WAXS spectra of mesoporous Al_2O_3-Mg-10 after Joule heating at 1155 °C, focusing on the zoomed-in angular ranges of 36° to 39° and 45° to 47° (refer to the right panels of Figure 4b). At the 3 s timepoint, the characteristic (311) spinel plane diffraction peak centered around 37.8° appeared. With increased annealing dwells, a shift of the diffraction peak to higher 2θ values was observed, reaching 38.2° at the 75 s timepoint (~1.1% increase). A similar trend was observed for the (400) spinel plane reflection, which shifted from approximately 46.1° to 46.4°.

Joule heating promoted the formation of a defect spinel structure with initially larger lattice constants. However, the lower Mg/Al composition in Al_2O_3-Mg-10 compared to a complete $MgAl_2O_4$ spinel structure (1:9 versus 1:2) resulted in unoccupied atomic sites and increased free volume in the lattice. To reduce thermodynamic instability during longer annealing dwells, the spinel lattice likely contracted, making its dimensions similar to the γ-Al_2O_3 structure. This is supported by the observation that mesoporous Al_2O_3-Mg samples with higher Mg loadings exhibited nonstoichiometric defect spinel structures with larger lattice constants (see Figure S6).

Figure 5a, along with Figures S7 and S8, display representative TEM images of mesoporous Al_2O_3-Mg-10 after Joule heating at 1155 °C for 3 s. HR-TEM and the bright-field TEM inset in Figure 5a present highly crystalline fringes within the parallel-aligned hexagonal mesopores, corroborating the SAXS and WAXS data in Figure 4. The selective area electron diffraction (SAED) pattern in Figure 5b and the corresponding 1D azimuthally integrated intensity plot in Figure 5c (and Table S1) display a sequence of characteristic diffraction reflections, affirming the presence of the $Mg_xAl_yO_4$ defect spinel crystal structure. Specifically, the identification of the (422) spinel plane, which is not easily identifiable in γ-Al_2O_3, further supports the structure interpretation.

Composition analyses via high-angle annular dark field scanning TEM (HAADF-STEM) and energy-dispersive X-ray spectroscopy (EDS) (Figures 5f and S9) and X-ray photoelectron spectroscopy (Figure S10) verified the uniform distribution of Al, Mg, and O elements, with a Mg/Al atomic percentage ratio close to 10:90. The nitrogen sorption isotherm in Figure S11 shows that the mesoporous Al_2O_3-Mg-10 sample had a Type IV isotherm with H2 hysteresis, indicating partial blockage in the pores, attributed to the carbon matrix derived from the thermopolymerized BCP.[5,32,33] The Brunauer–Emmett–Teller (BET) specific surface area, Barret–Joyner–Halenda (BJH) pore diameter and pore volume were approximately 168 m^2/g, 4.2 nm, and 015 cm^3/g, respectively.

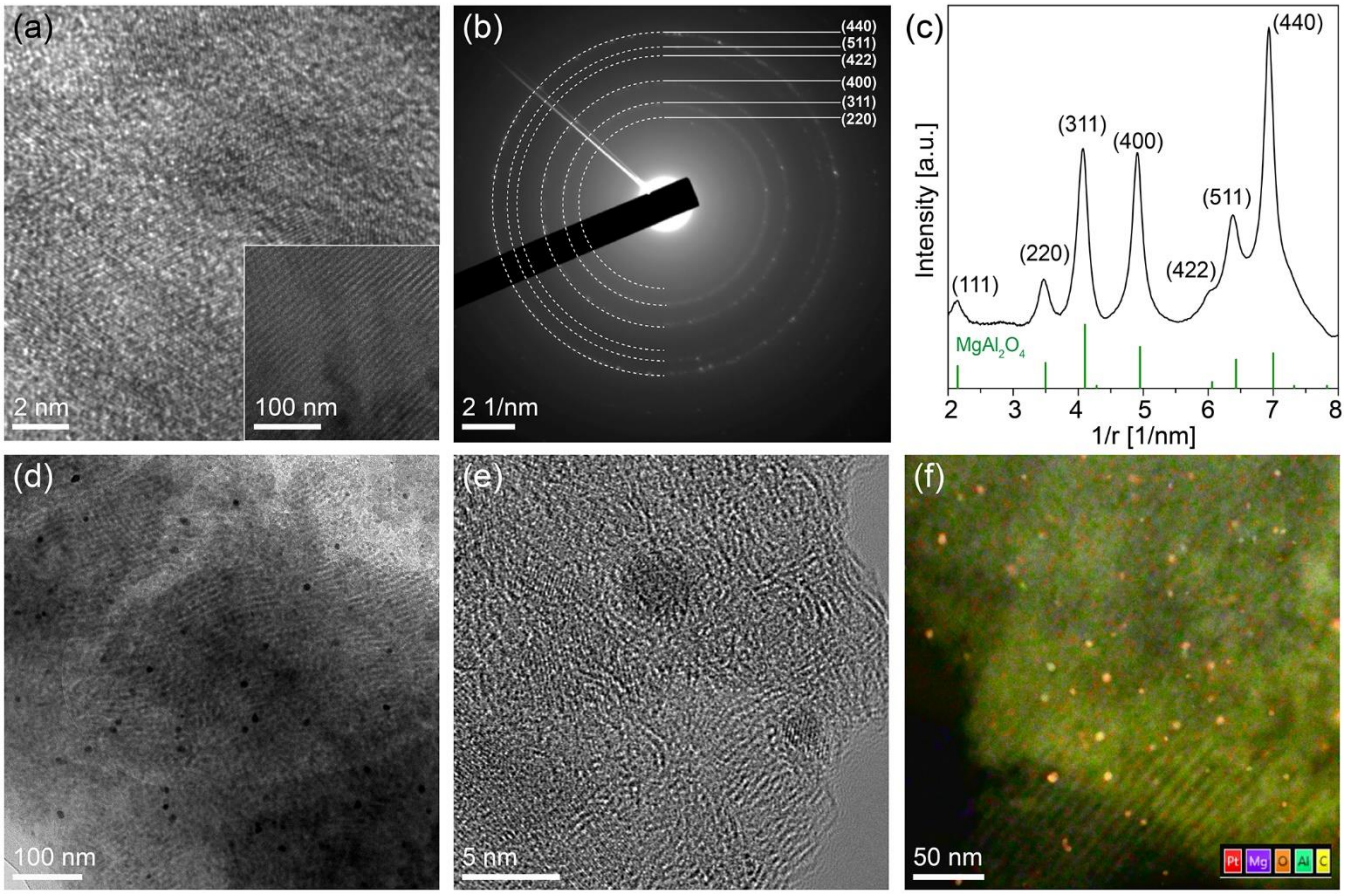

Figure 5. (a) HR-TEM and TEM (inset), (b) SAED profile and (c) azimuthally integrated intensity plot of mesoporous Al_2O_3-Mg-10 after Joule heating at 1155 °C for 3 s. (d) TEM, (e) HR-TEM and (f) HAADF-STEM EDS micrographs of ordered mesoporous 1wt%-Pt@$Mg_xAl_yO_4$ structures after Joule heating for 4 s. The expected reflections and relative intensities for the stoichiometric $MgAl_2O_4$ spinel structure (green, PDF 00-021-1152) are shown in (c).

To clarify the structure formation mechanism and kinetics of the nonstoichiometric $Mg_xAl_yO_4$ defect spinel crystal structures, we subjected the Al_2O_3-Mg-10 samples to isothermal Joule heating at temperatures of 1000, 1090 and 1155 °C. We estimated the average spinel crystallite size using the Scherrer equation, applied to the WAXS spectra of the isothermal samples (Figures 4 and S5) within the angular ranges of 37 to 38° and 46 to 47° (see Figure 6a). Subsequently, we

utilized the JMKA model (eqs. 2; see Figure 6b) and Arrhenius equation (eq. 5; see Figure 6c) to calculate the Avrami exponent *n*, rate constant *K*, and activation energy E_a. The summary of these values is presented in Table 1.

The formation of the mesoporous $Mg_xAl_yO_4$ defect spinel crystal structure induced by Joule heating aligned even more closely with the JMKA model under all three isothermal conditions (R^2 = 0.98–0.99). The derived Avrami exponents *n* and rate constants *K* for the different Joule heating temperatures, ranging from 0.63 to 0.73 and 0.19 to 0.42 s^{-1}, respectively, indicated instantaneous surface nucleation followed by diffusion-controlled growth of defect spinel crystallites.[47,51–53,55,56] This observation is consistent with the global fit analysis of the linearized JMKA model to all collected data, as shown in Figure S2b, which yielded global Avrami exponent *n* and rate constant *K* parameters of 0.53 and 0.42 s^{-1}, respectively. Intriguingly, the activation energy E_a of 34.7 kJ mol^{-1} was lower than that for the γ-Al_2O_3 system (49.4 kJ mol^{-1}). We postulate that the additional Mg atoms increase the number of heterogeneous nucleation sites, and the greater number of atomic vacancies along with a larger lattice free volume facilitate faster counter-diffusion of cations, thus favoring the formation of the defect spinel crystal structure under transient Joule heating.

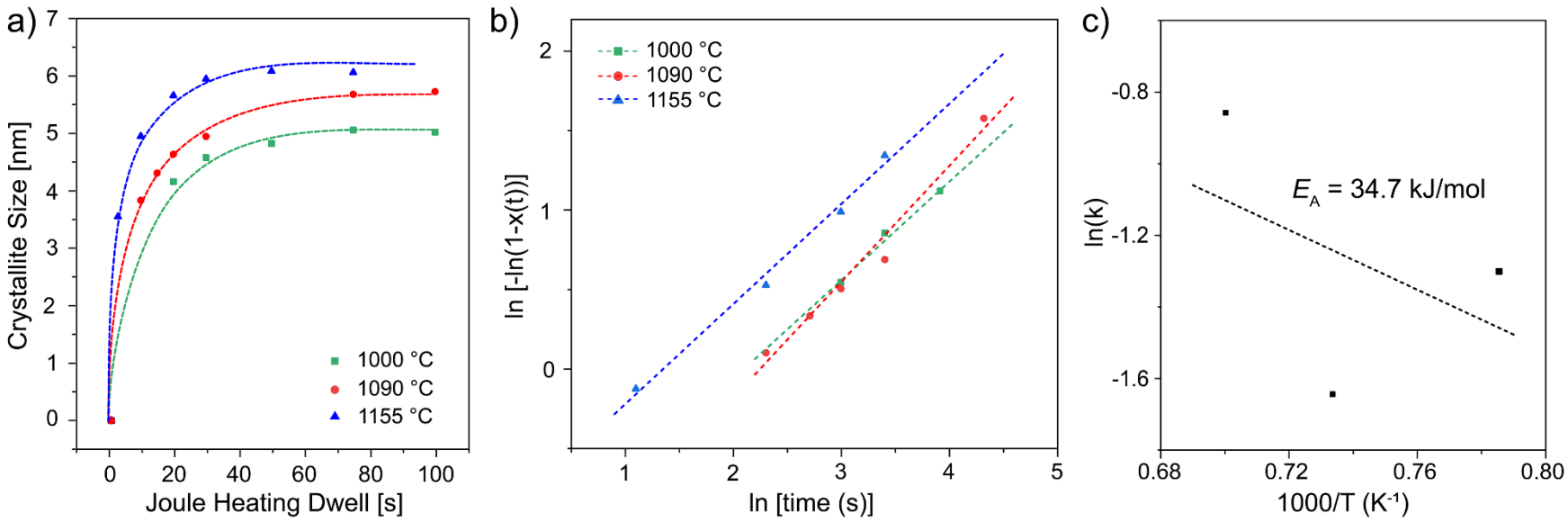

Figure 6 (a) Line plots tracking the growth of $Mg_xAl_yO_4$ defect spinel crystallites across various Joule heating temperatures and annealing times, as indicated, with dashed lines added to guide the eye. (b) Linearized JMKA model plots and (c) Arrhenius graph illustrating isothermal Joule heating-induced crystallization of ordered mesoporous $Mg_xAl_yO_4$ defect spinel samples at various temperatures, as indicated. The dashed lines were obtained from linear regression analysis of the respective data points.

The combination of solution synthesis (self-assembly) and rapid exposure to high temperatures for short dwells (Joule heating) enables an efficient approach to generate highly crystalline, periodically ordered mesoporous $Mg_xAl_yO_4$ defect spinel structures. This efficiency is attributed to several collective factors: (1) The solution preparation of Al-Mg sol additives and their selective interactions with the structure-directing copolymer help distribute Al^{3+} and Mg^{2+} cations uniformly throughout the ordered hexagonal cylindrical mesostructure. (2) The subsequent Joule heating process induces multiple synergetic reactions. Short pulses of extreme heat generate large populations of crystal defects, forming new diffusion pathways at the organic-inorganic boundaries and pore wall surfaces.[13,60] (3) The well-dispersed Al^{3+} and Mg^{2+} cations gain increased mobility at higher temperatures and only need to travel short distances to form the thermodynamically preferred defect spinel structure. (4) The defect spinel crystal lattices of nonstoichiometric Mg/Al compositions have more cationic defects and/or free spaces, likely to increase the diffusion of cations.[60,61] (5) The short annealing dwells and rapid thermal quenching further inhibit phase separation into other alternative crystalline metal oxides.[33,38–40,62–64]

We conducted further studies by comparing the WAXS spectra of Al_2O_3-Mg-20 and Al_2O_3-Mg-30 samples annealed by Joule heating for 3 to 15 s (see Figure S6) with the simulated crystal structures of $Mg_{0.388}Al_{2.408}O_4$ and γ-Al_2O_3 from published literature (Figure S12).[41,42] This analysis confirmed a high degree of congruence between our ordered mesoporous $Mg_xAl_yO_4$ defect spinel structures and the reference defect spinel structure of $Mg_{0.388}$ $Al_{2.408}O_4$. Although the fitting results can only be considered semi-quantitative due to the diffraction peaks having relatively low intensity and very broad profiles, which caused significant overlap of peaks from each phase, the results still clearly indicate the dominant phase within the samples to the first order. Hence, we cannot completely exclude the possibility that the resultant mesoporous Al_2O_3-Mg-10 after Joule heating may comprise of a solid solution consisting predominantly of the $Mg_xAl_yO_4$ phase and a minority γ-Al_2O_3 phase.

3.6 One-Pot Synthesis and Joule Heating of Pt@ Pt@$Mg_xAl_yO_4$ Structures

$Mg_xAl_yO_4$-based spinel is an excellent candidate for high-temperature catalyst and catalyst support due its high melting point, high chemical and thermal shock resistances, and low acidity.[16,30] Moreover, specific spinel crystal facets can help stabilize Pt nanoparticles during high-temperature sintering.[30] To this end, we prepared Pt@Al_2O_3-Mg-10 composites through a one-pot synthesis by adding dimethyl(cyclooctadiene)platinum together with the F127 copolymer and Al-Mg sol additives, forming a homogeneous solution mixture. The subsequent EISA step and Joule heating induced the formation of well-defined, crystalline mesoporous 5 wt%- and 1 wt%-loaded Pt@$Mg_xAl_yO_4$ structures.

SAXS patterns in Figure 7a corroborated that the mesoporous 5wt%-Pt@$Mg_xAl_yO_4$ structures retained their periodic *p*6*mm* lattice symmetry through all the processing steps: as-made (sample (i)), thermal curing (sample (ii)), and Joule heating at 1155 °C for 4 s (sample (iii)). WAXS verified the successful crystallization of Pt nanoparticles supported on the inner walls of mesoporous $Mg_xAl_yO_4$ hexagonal cylinders (sample (ii) in Figure 7b). This is evidenced by TEM and HR-TEM in Figure S13 depicting uniformly dispersed polycrystalline Pt nanoparticles, 5–10 nm in diameter, within the hexagonal cylinder mesopores. It is noted, however, that the broad WAXS diffraction peaks with low intensities around 38° and 46° likely represent convoluted reflections from Pt, $Mg_xAl_yO_4$ defect spinel, and γ-Al_2O_3, suggesting the Joule heating provided insufficient thermal energy to fully crystallize the $Mg_xAl_yO_4$ defect spinel structure, with some energy diverted to crystallize Pt nanoparticles instead.

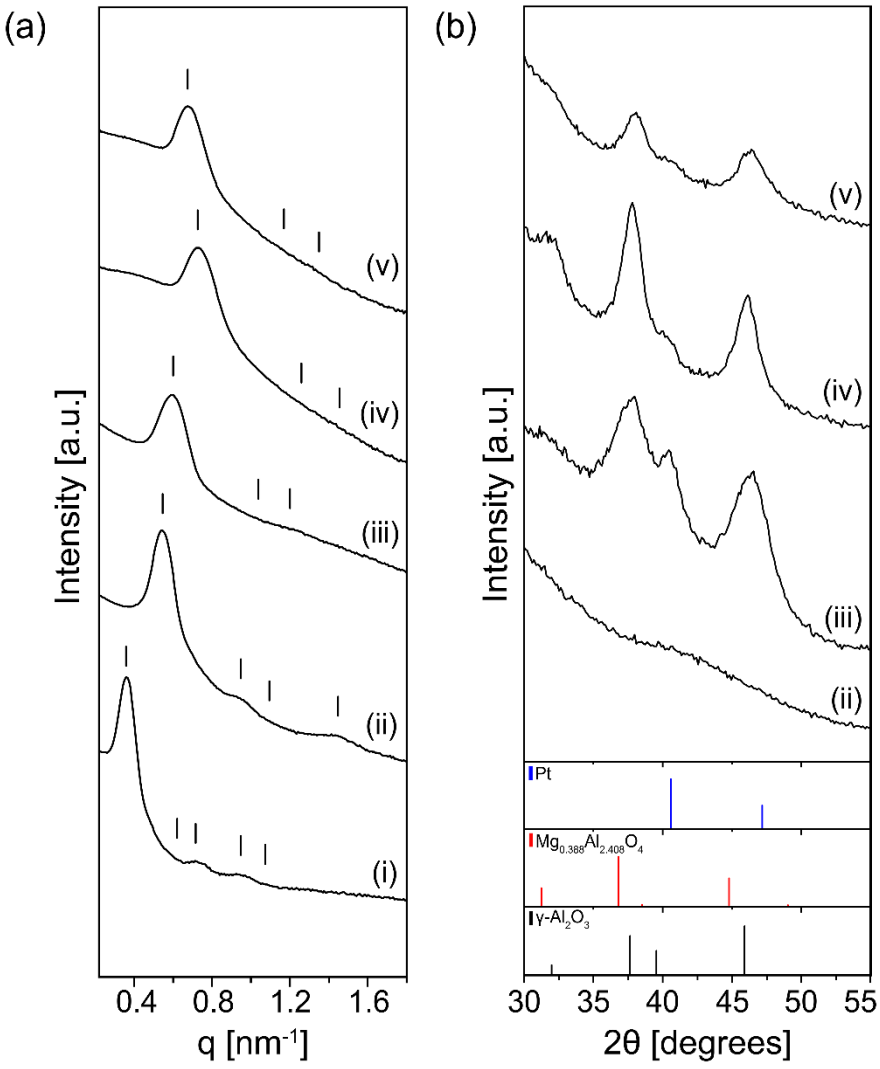

Figure 7 (a) SAXS and (b) WAXS patterns of ordered Pt@Al_2O_3-Mg-10 nanocomposites with different Pt compositions. Samples i to iii are that of the 5wt%-Pt loaded samples in the form of (i) as-made hybrid, (ii) thermally cured hybrid, and (iii) mesoporous 5wt%-Pt@$Mg_xAl_yO_4$ structures after Joule heating at 1155 °C for 4 s. Samples iv and v are that of the mesoporous 1wt%-Pt@$Mg_xAl_yO_4$ structures (iv) before and (v) after MCH dehydrogenation at 350 °C for over 16 h. Tick marks for the expected reflections of the *p*6*mm* symmetry are shown in (a). WAXS peak markings and relative intensities for Pt metal (blue, PDF 01-085-5658), $Mg_{0.388}Al_{2.408}O_4$ defect spinel (red, PDF 00-048-0528), and γ-Al_2O_3 (black, PDF 00-010-0425) are shown in (b).

Reducing the Pt loading to 1 wt% promoted a sparser distribution of Pt nanoparticles with smaller diameters ranging from 2 to 6 nm on the ordered mesoporous $Mg_xAl_yO_4$ structures as characterized by SAXS (sample (iv) in Figure 7a), WAXS (sample (iv) in Figure 7b), TEM (Figure 5d and S14), HR-TEM (Figure 5e) and HAADF-STEM EDS (Figure 5f and S9). Comparing samples (iii) and (iv) in Figure 7b, the WAXS reflection component assigned to the Pt (111) plane at $2\theta = 40.5°$ for 1wt%-Pt@$Mg_xAl_yO_4$ is noticeably less intense than that of the 5 wt% Pt-loaded sample. Compositional analyses of the 1wt%-Pt@$Mg_xAl_yO_4$ structures with EDS and XPS indicated that the Pt content was extremely low (<1 at%, see Figures S9 and S10).

We then evaluated the catalytic properties of mesoporous 1wt%-Pt@$Mg_xAl_yO_4$ for the dehydrogenation of methylcyclohexane (MCH) by flowing 3% MCH/nitrogen at 350 °C. Figure S15 illustrates that the catalyst initially exhibited a very low but steady MCH conversion of ~1.5% for the first 600 min, which then gradually decreased to ~0.7% after 1000 min. We speculate that MCH has very limited access to the active Pt nanoparticles due to the high carbon content in the mesoporous $Mg_xAl_yO_4$ scaffold that partially blocked the pores.[5,32,33] This is consistent with nitrogen sorption analysis indicating a significantly smaller specific surface area and pore volume of only 55 m^2/g and 0.056 cm^3/g, respectively (Figure S16). While the catalytic activity is far from optimal due to the Pt nanoparticles being sequestered within the F127-derived carbon matrix, the ordered mesoporous 1wt%-Pt@$Mg_xAl_yO_4$ exhibited excellent thermal and structural stability. This is corroborated by SAXS and WAXS (sample (v) in Figure 7a and b), along with TEM (Figure S17), indicating that the sample retained its mesoscale periodic order with minimal modifications to the crystallinity and Pt nanoparticle size. For future studies, the carbon matrix can be removed by either post-formation furnace calcination in air or chemical etching in oxidizing acids, facilitating the access of MCH to the Pt nanoparticles and increasing the overall catalytic activity and selectivity.

4. Conclusions

We have conducted an extensive investigation of the Joule heating-induced structure formation and kinetics in ordered mesoporous γ-Al_2O_3 and nonstoichiometric $Mg_xAl_yO_4$ defect spinel structures. Excellent fits to the JMKA model demonstrate that crystallization induced by Joule heating proceeds through instantaneous surface nucleation and diffusion-controlled crystallite growth. Our calculated activation energies for the Joule heating approach are significantly lower than those for conventional methods, which indicates enhanced reaction pathways and rapid transformation from amorphous to crystalline structures. We propose that Joule heating optimizes the reaction pathways by facilitating fast atomic mobility and reducing diffusion distances through the formation of new crystal defects and uniform dispersion of metal cations. In particular, Joule heating enables the rapid transformation of Al_2O_3-Mg-10 composites into a complete crystalline defect spinel structure at high temperatures within just a few seconds. Finally, the one-pot synthesis of refined Pt nanoparticles within the ordered mesoporous Al_2O_3-Mg scaffolds, exhibiting high thermal and structural stability under thermal catalysis redox conditions, paves the way for developing high-surface-area and thermochemically resistant catalyst systems.

Acknowledgements

This work was supported by a Singapore Ministry of Education AcRF Tier 2 grant (MOE-T2EP50221-0017) and a member-directed research grant from ExxonMobil through the Singapore Energy Center (EM11161.TO6). This work made use of research facilities at the Facility for Analysis, Characterization, Testing and Simulation (FACTS), Nanyang Technological University, Singapore. This work was authored in part by the National Renewable Energy Laboratory, operated by Alliance for Sustainable Energy, LLC, for the U.S. Department of Energy (DOE) under Contract No. DE-AC36-08GO28308. The views expressed in the article do

not necessarily represent the views of the DOE or the U.S. Government. The authors gratefully acknowledge H Roslie and S.F. Tan for helpful discussion.

References:

(1) Xu, X.; Megarajan, S. K.; Zhang, Y.; Jiang, H. Ordered Mesoporous Alumina and Their Composites Based on Evaporation Induced Self-Assembly for Adsorption and Catalysis. *Chem. Mater.* **2020**, *32* (1), 3–26. https://doi.org/10.1021/acs.chemmater.9b03873.

(2) Niesz, K.; Yang, P.; Somorjai, G. A. Sol-Gel Synthesis of Ordered Mesoporous Alumina. *Chem. Commun.* **2005**, No. 15, 1986–1987. https://doi.org/10.1039/B419249D.

(3) Yuan, Q.; Yin, A.-X.; Luo, C.; Sun, L.-D.; Zhang, Y.-W.; Duan, W.-T.; Liu, H.-C.; Yan, C.-H. Facile Synthesis for Ordered Mesoporous γ-Aluminas with High Thermal Stability. *J. Am. Chem. Soc.* **2008**, *130* (11), 3465–3472. https://doi.org/10.1021/ja0764308.

(4) Wu, Z.; Li, Q.; Feng, D.; Webley, P. A.; Zhao, D. Ordered Mesoporous Crystalline γ-Al_2O_3 with Variable Architecture and Porosity from a Single Hard Template. *J. Am. Chem. Soc.* **2010**, *132* (34), 12042–12050. https://doi.org/10.1021/ja104379a.

(5) Tan, K. W.; Sai, H.; Robbins, S. W.; Werner, J. G.; Hoheisel, T. N.; Hesse, S. A.; Beaucage, P. A.; DiSalvo, F. J.; Gruner, S. M.; Murtagh, M.; Wiesner, U. Ordered Mesoporous Crystalline Aluminas from Self-Assembly of ABC Triblock Terpolymer–Butanol–Alumina Sols. *RSC Adv.* **2015**, *5* (61), 49287–49294. https://doi.org/10.1039/C5RA07421E.

(6) Seah, G. L.; Wang, L.; Tan, L. F.; Tipjanrawee, C.; Sasangka, W. A.; Usadi, A. K.; McConnachie, J. M.; Tan, K. W. Ordered Mesoporous Alumina with Tunable Morphologies and Pore Sizes for CO_2 Capture and Dye Separation. *ACS Appl. Mater. Interfaces* **2021**, *13* (30), 36117–36129. https://doi.org/10.1021/acsami.1c06151.

(7) Zhang, Z.; Zhu, Y.; Asakura, H.; Zhang, B.; Zhang, J.; Zhou, M.; Han, Y.; Tanaka, T.; Wang, A.; Zhang, T.; Yan, N. Thermally Stable Single Atom Pt/m-Al_2O_3 for Selective Hydrogenation and CO Oxidation. *Nat. Commun.* **2017**, *8* (1), 16100. https://doi.org/10.1038/ncomms16100.

(8) Li, J.; Li, R.; Wang, W.; Lan, K.; Zhao, D. Ordered Mesoporous Crystalline Frameworks Toward Promising Energy Applications. *Adv. Mater.* **2024**, 2311460. https://doi.org/10.1002/adma.202311460.

(9) Morris, S. M.; Fulvio, P. F.; Jaroniec, M. Ordered Mesoporous Alumina-Supported Metal Oxides. *J. Am. Chem. Soc.* **2008**, *130* (45), 15210–15216. https://doi.org/10.1021/ja806429q.

(10) Cai, W.; Yu, J.; Anand, C.; Vinu, A.; Jaroniec, M. Facile Synthesis of Ordered Mesoporous Alumina and Alumina-Supported Metal Oxides with Tailored Adsorption and Framework Properties. *Chem. Mater.* **2011**, *23* (5), 1147–1157. https://doi.org/10.1021/cm102512v.

(11) Li, W.; Chen, D.; Xia, F.; Tan, J. Z. Y.; Huang, P.-P.; Song, W.-G.; Nursam, N. M.; Caruso, R. A. Extremely High Arsenic Removal Capacity for Mesoporous Aluminium Magnesium Oxide Composites. *Environ. Sci.: Nano* **2016**, *3* (1), 94–106. https://doi.org/10.1039/C5EN00171D.

(12) Pan, D.; Dong, Z.; He, M.; Chen, W.; Chen, S.; Yu, F.; Fan, B.; Cui, X.; Li, R. Structural and Surface Properties of Highly Ordered Mesoporous Magnesium-Aluminium Composite Oxides Derived from Facile Synthesis. *Mater. Chem. Phys.* **2017**, *186*, 574–583. https://doi.org/10.1016/j.matchemphys.2016.11.038.

(13) Gonçalves, A. A. S.; Costa, M. J. F.; Zhang, L.; Ciesielczyk, F.; Jaroniec, M. One-Pot Synthesis of MeAl2O4 (Me = Ni, Co, or Cu) Supported on γ-Al2O3 with Ultralarge Mesopores: Enhancing Interfacial Defects in γ-Al_2O_3 To Facilitate the Formation of Spinel Structures at Lower Temperatures. *Chem. Mater.* **2018**, *30* (2), 436–446. https://doi.org/10.1021/acs.chemmater.7b04353.

(14) Cho, E.; Lee, Y.-H.; Kim, H.; Jang, E. J.; Kwak, J. H.; Lee, K.; Ko, C. H.; Yoon, W. L. Ni Catalysts for Dry Methane Reforming Prepared by A-Site Exsolution on Mesoporous Defect Spinel Magnesium Aluminate. *Appl. Catal., A* **2020**, *602*, 117694. https://doi.org/10.1016/j.apcata.2020.117694.

(15) Baudín, C.; Martínez, R.; Pena, P. High-Temperature Mechanical Behavior of Stoichiometric Magnesium Spinel. *J. Am. Ceram. Soc.* **1995**, *78* (7), 1857–1862. https://doi.org/10.1111/j.1151-2916.1995.tb08900.x.

(16) Ganesh, I. A Review on Magnesium Aluminate ($MgAl_2O_4$) Spinel: Synthesis, Processing and Applications. *Int. Mater. Rev.* **2013**, *58* (2), 63–112. https://doi.org/10.1179/1743280412Y.0000000001.

(17) Alvar, E. N.; Rezaei, M. Mesoporous Nanocrystalline MgAl2O4 Spinel and Its Applications as Support for Ni Catalyst in Dry Reforming. *Scripta Materialia* **2009**, *61* (2), 212–215. https://doi.org/10.1016/j.scriptamat.2009.03.047.

(18) Kresge, C. T.; Leonowicz, M. E.; Roth, W. J.; Vartuli, J. C.; Beck, J. S. Ordered Mesoporous Molecular Sieves Synthesized by a Liquid-Crystal Template Mechanism. *Nature* **1992**, *359* (6397), 710–712. https://doi.org/10.1038/359710a0.

(19) Zhao, D.; Feng, J.; Huo, Q.; Melosh, N.; Fredrickson, G. H.; Chmelka, B. F.; Stucky, G. D. Triblock Copolymer Syntheses of Mesoporous Silica with Periodic 50 to 300 Angstrom Pores. *Science* **1998**, *279* (5350), 548–552. https://doi.org/10.1126/science.279.5350.548.

(20) Yang, P.; Zhao, D.; Margolese, D. I.; Chmelka, B. F.; Stucky, G. D. Generalized Syntheses of Large-Pore Mesoporous Metal Oxides with Semicrystalline Frameworks. *Nature* **1998**, *396* (6707), 152–155. https://doi.org/10.1038/24132.

(21) Meng, Y.; Gu, D.; Zhang, F.; Shi, Y.; Yang, H.; Li, Z.; Yu, C.; Tu, B.; Zhao, D. Ordered Mesoporous Polymers and Homologous Carbon Frameworks: Amphiphilic Surfactant Templating and Direct Transformation. *Angew. Chem., Int. Ed.* **2005**, *44* (43), 7053–7059. https://doi.org/10.1002/anie.200501561.

(22) Arora, H.; Du, P.; Tan, K. W.; Hyun, J. K.; Grazul, J.; Xin, H. L.; Muller, D. A.; Thompson, M. O.; Wiesner, U. Block Copolymer Self-Assembly–Directed Single-Crystal Homo- and Heteroepitaxial Nanostructures. *Science* **2010**, *330* (6001), 214–219. https://doi.org/10.1126/science.1193369.

(23) Sai, H.; Tan, K. W.; Hur, K.; Asenath-Smith, E.; Hovden, R.; Jiang, Y.; Riccio, M.; Muller, D. A.; Elser, V.; Estroff, L. A.; Gruner, S. M.; Wiesner, U. Hierarchical Porous Polymer Scaffolds from Block Copolymers. *Science* **2013**, *341* (6145), 530–534. https://doi.org/10.1126/science.1238159.

(24) Tan, K. W.; Jung, B.; Werner, J. G.; Rhoades, E. R.; Thompson, M. O.; Wiesner, U. Transient Laser Heating Induced Hierarchical Porous Structures from Block Copolymer–

Directed Self-Assembly. *Science* **2015**, *349* (6243), 54–58. https://doi.org/10.1126/science.aab0492.

(25) Zhang, Q.; Matsuoka, F.; Suh, H. S.; Beaucage, P. A.; Xiong, S.; Smilgies, D.-M.; Tan, K. W.; Werner, J. G.; Nealey, P. F.; Wiesner, U. B. Pathways to Mesoporous Resin/Carbon Thin Films with Alternating Gyroid Morphology. *ACS Nano* **2018**, *12* (1), 347–358. https://doi.org/10.1021/acsnano.7b06436.

(26) Tu, W. H.; Seah, G. L.; Li, Y.; Wang, X.; Tan, K. W. Transient Laser-Annealing-Induced Mesophase Transitions of Block Copolymer–Resol Thin Films. *ACS Polym. Au* **2022**, *2* (1), 42–49. https://doi.org/10.1021/acspolymersau.1c00040.

(27) Li, Y.; Tiwari, A. K.; Ng, J. S.; Seah, G. L.; Lim, H. K.; Suteewong, T.; Tay, C. Y.; Lam, Y. M.; Tan, K. W. One-Pot Synthesis of Aminated Bimodal Mesoporous Silica Nanoparticles as Silver-Embedded Antibacterial Nanocarriers and CO_2 Capture Sorbents. *ACS Appl. Mater. Interfaces* **2022**, *14* (46), 52279–52288. https://doi.org/10.1021/acsami.2c13076.

(28) Tan, K. W.; Wiesner, U. Block Copolymer Self-Assembly Directed Hierarchically Structured Materials from Nonequilibrium Transient Laser Heating. *Macromolecules* **2019**, *52* (2), 395–409. https://doi.org/10.1021/acs.macromol.8b01766.

(29) Guo, J.; Lou, H.; Zhao, H.; Chai, D.; Zheng, X. Dry Reforming of Methane over Nickel Catalysts Supported on Magnesium Aluminate Spinels. *Appl. Catal., A* **2004**, *273* (1–2), 75–82. https://doi.org/10.1016/j.apcata.2004.06.014.

(30) Li, W.-Z.; Kovarik, L.; Mei, D.; Liu, J.; Wang, Y.; Peden, C. H. F. Stable Platinum Nanoparticles on Specific $MgAl_2O_4$ Spinel Facets at High Temperatures in Oxidizing Atmospheres. *Nat. Commun.* **2013**, *4* (1), 2481. https://doi.org/10.1038/ncomms3481.

(31) Ganesh, I.; Srinivas, B.; Johnson, R.; Saha, B. P.; Mahajan, Y. R. Microwave Assisted Solid State Reaction Synthesis of MgAl2O4 Spinel Powders. *J. Eur. Ceram. Soc.* **2004**, *24* (2), 201–207. https://doi.org/10.1016/S0955-2219(03)00602-2.

(32) Lee, J.; Orilall, M. C.; Warren, S. C.; Kamperman, M.; DiSalvo, F. J.; Wiesner, U. Direct Access to Thermally Stable and Highly Crystalline Mesoporous Transition-Metal Oxides with Uniform Pores. *Nat. Mater.* **2008**, *7* (3), 222–228. https://doi.org/10.1038/nmat2111.

(33) Wang, L.; Seah, G. L.; Li, Y.; Tu, W. H.; Manalastas Jr., W.; Reavley, M. J.-H.; Corcoran Jr., E. W.; Usadi, A. K.; Du, Z.; Madhavi, S.; McConnachie, J. M.; Ong, H. G.; Tan, K. W. Ultrafast Crystallization of Ordered Mesoporous Metal Oxides and Carbon from Block Copolymer Self-Assembly and Joule Heating. *Adv. Mater. Interfaces* **2022**, *9* (19), 2200151. https://doi.org/10.1002/admi.202200151.

(34) Shi, W.; Li, Z.; Gong, Z.; Liang, Z.; Liu, H.; Han, Y.-C.; Niu, H.; Song, B.; Chi, X.; Zhou, J.; Wang, H.; Xia, B. Y.; Yao, Y.; Tian, Z.-Q. Transient and General Synthesis of High-Density and Ultrasmall Nanoparticles on Two-Dimensional Porous Carbon via Coordinated Carbothermal Shock. *Nat. Commun.* **2023**, *14* (1), 2294. https://doi.org/10.1038/s41467-023-38023-5.

(35) Ding, X.; He, Z.; Li, J.; Xu, X.; Li, Z. Carbon Carrier-Based Rapid Joule Heating Technology: A Review on the Preparation and Applications of Functional Nanomaterials. *Nanoscale* **2024**, *16* (26), 12309–12328. https://doi.org/10.1039/D4NR01510J.

(36) Ge, Y.; Huang, B.; Li, L.; Yun, Q.; Shi, Z.; Chen, B.; Zhang, H. Structural Transformation of Unconventional-Phase Materials. *ACS Nano* **2023**, *17* (14), 12935–12954. https://doi.org/10.1021/acsnano.3c01922.

(37) Ma, J.; Xia, C.; Salim, T.; Tay, Y. Y.; Wong, L. H.; Tan, K. W. Ultrafast Joule Heating-Induced Formation of Amorphous CoFeNi Phosphate for Efficient and Stable Oxygen Evolution Reaction. *J. Mater. Chem. A* **2024**. https://doi.org/10.1039/D4TA03130J.

(38) Yao, Y.; Huang, Z.; Xie, P.; Lacey, S. D.; Jacob, R. J.; Xie, H.; Chen, F.; Nie, A.; Pu, T.; Rehwoldt, M.; Yu, D.; Zachariah, M. R.; Wang, C.; Shahbazian-Yassar, R.; Li, J.; Hu, L. Carbothermal Shock Synthesis of High-Entropy-Alloy Nanoparticles. *Science* **2018**, *359* (6383), 1489–1494. https://doi.org/10.1126/science.aan5412.

(39) Wang, C.; Ping, W.; Bai, Q.; Cui, H.; Hensleigh, R.; Wang, R.; Brozena, A. H.; Xu, Z.; Dai, J.; Pei, Y.; Zheng, C.; Pastel, G.; Gao, J.; Wang, X.; Wang, H.; Zhao, J.-C.; Yang, B.; Zheng, X. (Rayne); Luo, J.; Mo, Y.; Dunn, B.; Hu, L. A General Method to Synthesize and Sinter Bulk Ceramics in Seconds. *Science* **2020**, *368* (6490), 521–526. https://doi.org/10.1126/science.aaz7681.

(40) Xie, H.; Liu, N.; Zhang, Q.; Zhong, H.; Guo, L.; Zhao, X.; Li, D.; Liu, S.; Huang, Z.; Lele, A. D.; Brozena, A. H.; Wang, X.; Song, K.; Chen, S.; Yao, Y.; Chi, M.; Xiong, W.; Rao, J.; Zhao, M.; Shneider, M. N.; Luo, J.; Zhao, J.-C.; Ju, Y.; Hu, L. A Stable Atmospheric-Pressure Plasma for Extreme-Temperature Synthesis. *Nature* **2023**, *623* (7989), 964–971. https://doi.org/10.1038/s41586-023-06694-1.

(41) Basso, R.; Carbonin, S.; Giusta, A. D. Cation and vacancy distribution in a synthetic defect spinel. *Z. Kristallogr. Cryst. Mater.* **1991**, *194* (1–4), 111–120. https://doi.org/10.1524/zkri.1991.194.14.111.

(42) Zhou, R.-S.; Snyder, R. L. Structures and Transformation Mechanisms of the η, γ and θ Transition Aluminas. *Acta Crystallogr., Sect. B: Struct. Sci.* **1991**, *47* (5), 617–630. https://doi.org/10.1107/S0108768191002719.

(43) Brunauer, S.; Emmett, P. H.; Teller, E. Adsorption of Gases in Multimolecular Layers. *J. Am. Chem. Soc.* **1938**, *60* (2), 309–319.

(44) Barrett, E. P.; Joyner, L. G.; Halenda, P. P. The Determination of Pore Volume and Area Distributions in Porous Substances. I. Computations from Nitrogen Isotherms. *J. Am. Chem. Soc.* **1951**, *73* (1), 373–380. https://doi.org/10.1021/ja01145a126.

(45) Kruk, M.; Jaroniec, M.; Sayari, A. Application of Large Pore MCM-41 Molecular Sieves to Improve Pore Size Analysis Using Nitrogen Adsorption Measurements. *Langmuir* **1997**, *13* (23), 6267–6273. https://doi.org/10.1021/la970776m.

(46) Orilall, M. C.; Matsumoto, F.; Zhou, Q.; Sai, H.; Abruña, H. D.; DiSalvo, F. J.; Wiesner, U. One-Pot Synthesis of Platinum-Based Nanoparticles Incorporated into Mesoporous Niobium Oxide−Carbon Composites for Fuel Cell Electrodes. *J. Am. Chem. Soc.* **2009**, *131* (26), 9389–9395. https://doi.org/10.1021/ja903296r.

(47) Kirsch, B. L.; Richman, E. K.; Riley, A. E.; Tolbert, S. H. In-Situ X-Ray Diffraction Study of the Crystallization Kinetics of Mesoporous Titania Films. *J. Phys. Chem. B* **2004**, *108* (34), 12698–12706. https://doi.org/10.1021/jp036442p.

(48) Moore, D. T.; Sai, H.; Tan, K. W.; Smilgies, D.-M.; Zhang, W.; Snaith, H. J.; Wiesner, U.; Estroff, L. A. Crystallization Kinetics of Organic–Inorganic Trihalide Perovskites and the Role of the Lead Anion in Crystal Growth. *J. Am. Chem. Soc.* **2015**, *137* (6), 2350–2358. https://doi.org/10.1021/ja512117e.
(49) Johnson, W.; Mehl, R. Reaction Kinetics in Processes of Nucleation and Growth. *Trans ALME* **1939**, *135*, 416–442.
(50) Avrami, M. Kinetics of Phase Change. I General Theory. *J. Chem. Phys.* **1939**, *7* (12), 1103–1112. https://doi.org/10.1063/1.1750380.
(51) Cantor, B. The Avrami Equation: Phase Transformations. In *The Equations of Materials*; Cantor, B., Ed.; Oxford University Press, 2020; p 0. https://doi.org/10.1093/oso/9780198851875.003.0009.
(52) Jhung, S. H.; Jin, T.; Hwang, Y. K.; Chang, J.-S. Microwave Effect in the Fast Synthesis of Microporous Materials: Which Stage Between Nucleation and Crystal Growth Is Accelerated by Microwave Irradiation? *Chem. Eur. J.* **2007**, *13* (16), 4410–4417. https://doi.org/10.1002/chem.200700098.
(53) Xia, X.; Vogt, B. D. Microwave Processing Controls the Morphology of Block Copolymer-Templated Mesoporous Cobalt Oxide Films. *Langmuir* **2020**, *36* (5), 1288–1297. https://doi.org/10.1021/acs.langmuir.9b03138.
(54) Simpson, T. W.; Wen, Q.; Yu, N.; Clarke, D. R. Kinetics of the Amorphous →γ→α Transformations in Aluminum Oxide: Effect of Crystallographic Orientation. *J. Am. Ceram. Soc*. **2005**, *81* (1), 61–66. https://doi.org/10.1111/j.1151-2916.1998.tb02296.x.
(55) Zhang, H.; Banfield, J. F. Phase Transformation of Nanocrystalline Anatase-to-Rutile via Combined Interface and Surface Nucleation. *J. Mater. Res.* **2000**, *15* (2), 437–448. https://doi.org/10.1557/JMR.2000.0067.
(56) Zhang, H.; Banfield, J. F. Kinetics of Crystallization and Crystal Growth of Nanocrystalline Anatase in Nanometer-Sized Amorphous Titania. *Chem. Mater.* **2002**, *14* (10), 4145–4154. https://doi.org/10.1021/cm020072k.
(57) Fan, J.; Boettcher, S. W.; Stucky, G. D. Nanoparticle Assembly of Ordered Multicomponent Mesostructured Metal Oxides via a Versatile Sol−Gel Process. *Chem. Mater.* **2006**, *18* (26), 6391–6396. https://doi.org/10.1021/cm062359d.
(58) Samain, L.; Jaworski, A.; Edén, M.; Ladd, D. M.; Seo, D.-K.; Javier Garcia-Garcia, F.; Häussermann, U. Structural Analysis of Highly Porous γ-Al_2O_3. *J. Solid State Chem.* **2014**, *217*, 1–8. https://doi.org/10.1016/j.jssc.2014.05.004.
(59) Navrotsky, A.; Wechsler, B. A.; Geisinger, K.; Seifert, F. Thermochemistry of MgAl2O4-Al8/3O4 Defect Spinels. *Journal of the American Ceramic Society* **1986**, *69* (5), 418–422. https://doi.org/10.1111/j.1151-2916.1986.tb04772.x.
(60) Feng, B.; Ishikawa, R.; Kumamoto, A.; Shibata, N.; Ikuhara, Y. Atomic Scale Origin of Enhanced Ionic Conductivity at Crystal Defects. *Nano Lett.* **2019**, *19* (3), 2162–2168. https://doi.org/10.1021/acs.nanolett.9b00506.

(61) Murphy, S. T.; Gilbert, C. A.; Smith, R.; Mitchell, T. E.; Grimes, R. W. Non-Stoichiometry in $MgAl_2O_4$ Spinel. *Philos. Mag.* **2010**, *90* (10), 1297–1305. https://doi.org/10.1080/14786430903341402.

(62) Li, Y.; Tay, Y. Y.; Buenconsejo, P. J. S.; Manalastas Jr., W.; Tu, W. H.; Lim, H. K.; Salim, T.; Thompson, M. O.; Madhavi, S.; Tay, C. Y.; Tan, K. W. Laser Annealing-Induced Phase Transformation Behaviors of High Entropy Metal Alloy, Oxide, and Nitride Nanoparticle Combinations. *Adv. Funct. Mater.* **2023**, *33* (13), 2211279. https://doi.org/10.1002/adfm.202211279.

(63) Cui, X.; Liu, Y.; Wang, X.; Tian, X.; Wang, Y.; Zhang, G.; Liu, T.; Ding, J.; Hu, W.; Chen, Y. Rapid High-Temperature Liquid Shock Synthesis of High-Entropy Alloys for Hydrogen Evolution Reaction. *ACS Nano* **2024**, *18* (4), 2948–2957. https://doi.org/10.1021/acsnano.3c07703.

(64) Ahn, J.; Park, S.; Oh, D.; Lim, Y.; Nam, J. S.; Kim, J.; Jung, W.; Kim, I.-D. Rapid Joule Heating Synthesis of Oxide-Socketed High-Entropy Alloy Nanoparticles as CO2 Conversion Catalysts. *ACS Nano* **2023**, *17* (13), 12188–12199. https://doi.org/10.1021/acsnano.3c00443.

Supporting Information

Rapid Joule Heating-Induced Structural Evolution of Nonstoichiometric Ordered Mesoporous Aluminum-Based Spinel Structures

Leyan Wang,[1] Qihang Chen,[1] Yong Quan Yeo,[1] Geok Leng Seah,[1] Hossein Akhoundzadeh,[2] Yee Yan Tay,[1] Teddy Salim,[1] Pio J. S. Buenconsejo,[1] Edward W. Corcoran Jr.,[3] Adam K. Usadi,[3] Jonathan M. McConnachie,[3] David T. Moore,[4] Rong Xu,[2] Zhong Chen,[1] and Kwan W. Tan[1,*]

Affiliations:

[1]School of Materials Science and Engineering, Nanyang Technological University, Singapore 639798, Singapore.

[2]School of School of Chemistry, Chemical Engineering and Biotechnology, Nanyang Technological University, Singapore 637459, Singapore.

[3]ExxonMobil Techology and Engineering Company, Annandale, New Jersey 08801, United States.

[4]Materials Chemistry & Computation Sciences, National Renewable Energy Laboratory, Golden, Colorado 80401, United States.

*Correspondence: kwtan@ntu.edu.sg

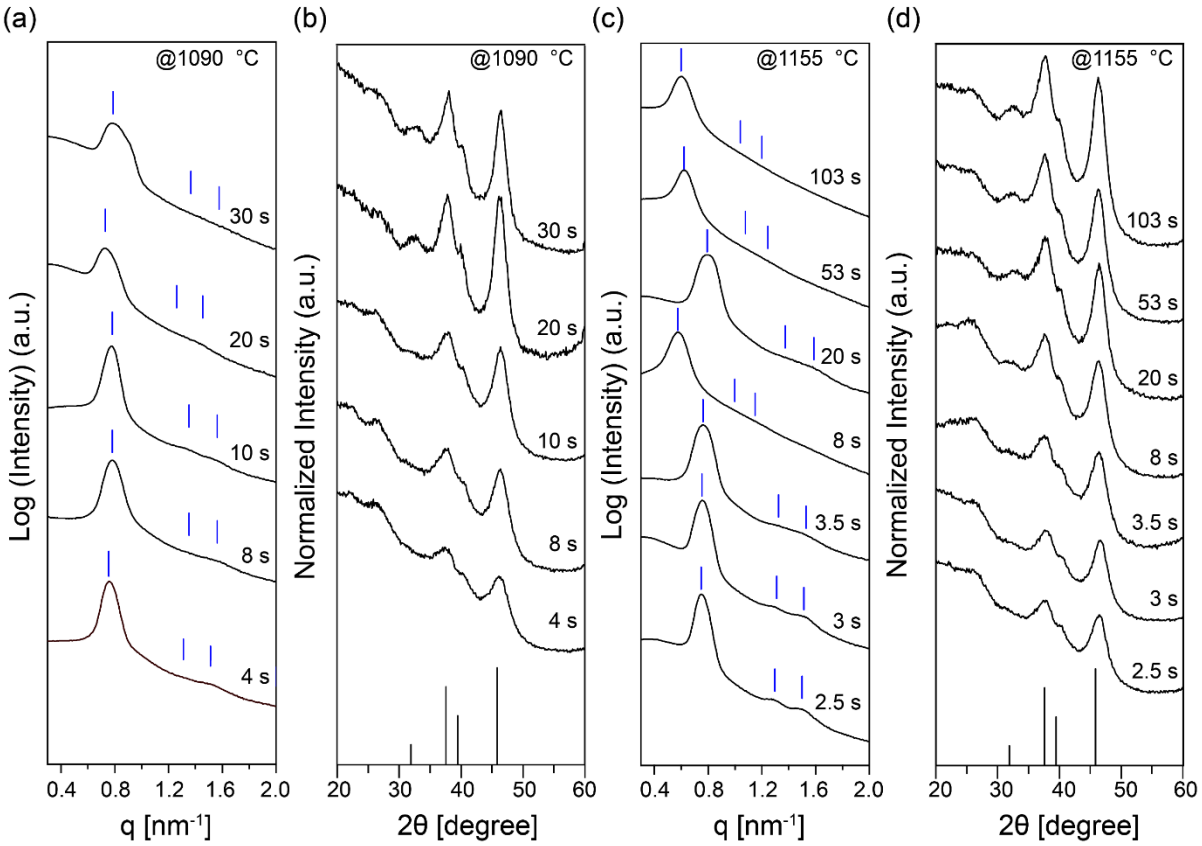

Figure S1. (a, c) SAXS and (b, d) WAXS patterns of mesoporous γ-Al_2O_3 samples after Joule heating at 1090 °C (a, b) and 1155 °C (c, d) for various durations as indicated. Tick marks (blue) for the expected reflections of the *p6mm* symmetry are shown in (a, c). WAXS peak markings and relative intensities (black) for γ-Al_2O_3 (PDF-00-010-0425) are shown in (b, d).

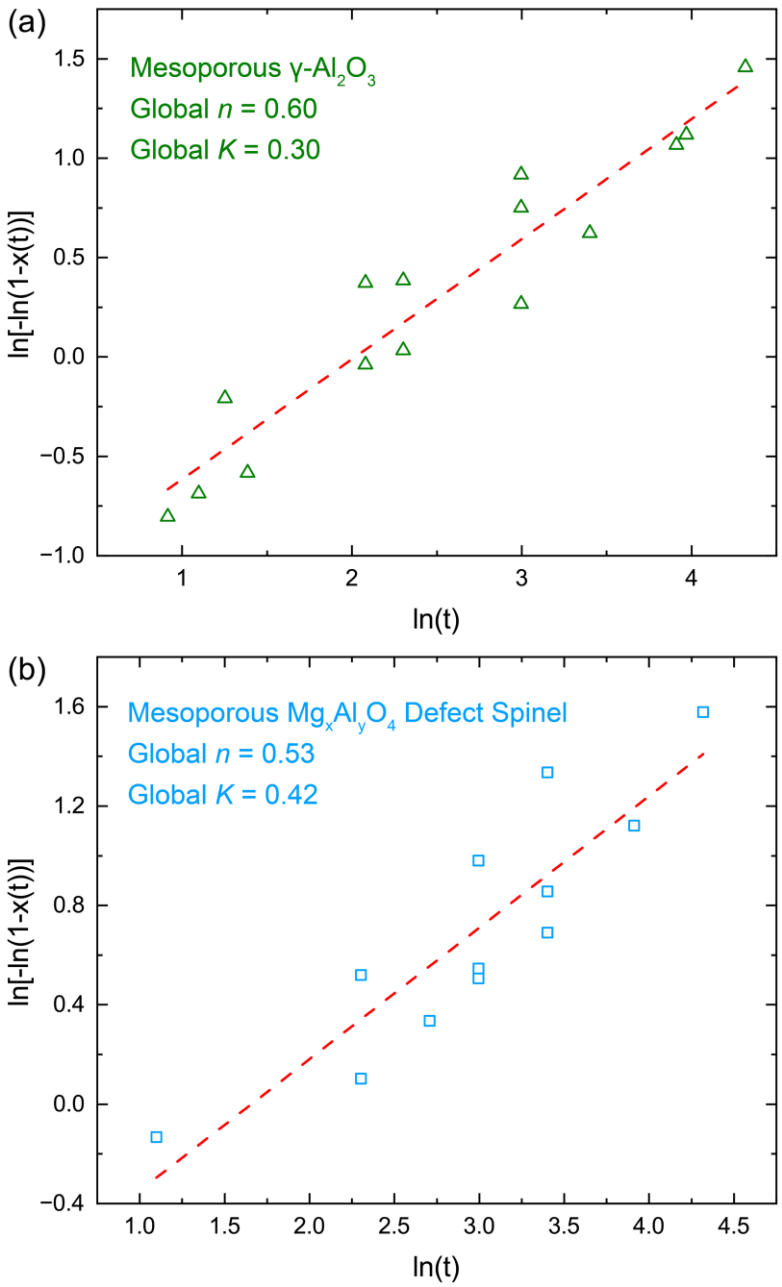

Figure S2. Global fits of linearized JMKA model plots of (a) mesoporous γ-Al_2O_3 and (b) mesoporous Al_2O_3-Mg-10 samples subjected to Joule heating at isothermal temperatures of 1000, 1090 and 1155 °C.

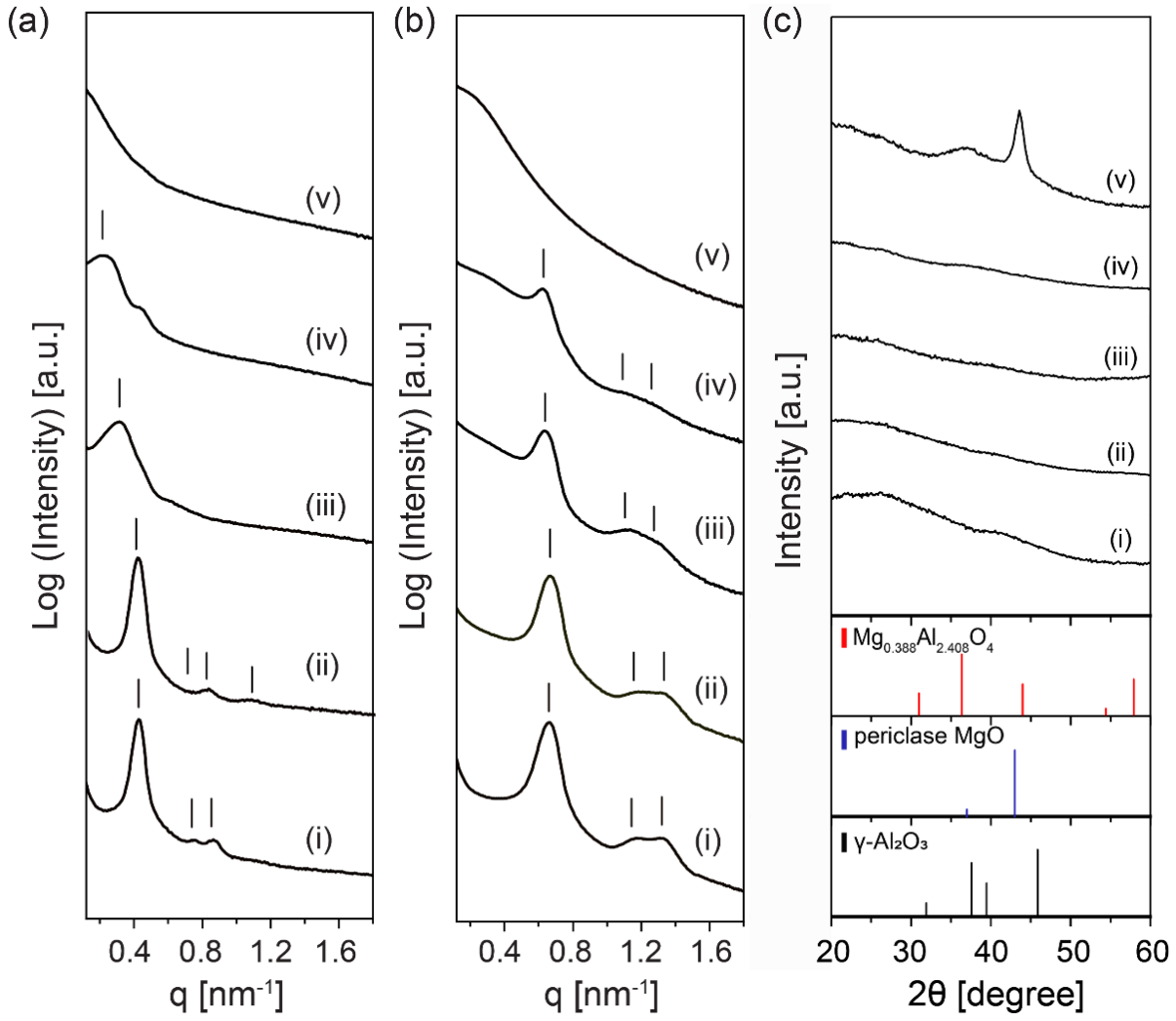

Figure S3. (a, b) SAXS and (c) WAXS patterns of F127-Al_2O_3-Mg samples in the form of thermally cured hybrids (a) and corresponding mesoporous Al_2O_3-Mg structures after furnace calcination in air at 450 °C (b, c). The mixed oxide samples with different Mg contents are (i) Al_2O_3-Mg-05, (ii) Al_2O_3-Mg-10, (iii) Al_2O_3-Mg-20, (iv) Al_2O_3-Mg-30 and (v) Al_2O_3-Mg-50. Tick marks (blue) for the expected reflections of the *p6mm* symmetry are shown in (a, b). WAXS peak markings and relative intensities for γ-Al_2O_3 (black, PDF-00-010-0425), periclase MgO (blue, PDF-04-002-3057), and $Mg_{0.388}Al_{2.408}O_4$ defect spinel (red, PDF-00-048-0528) are shown in (c).

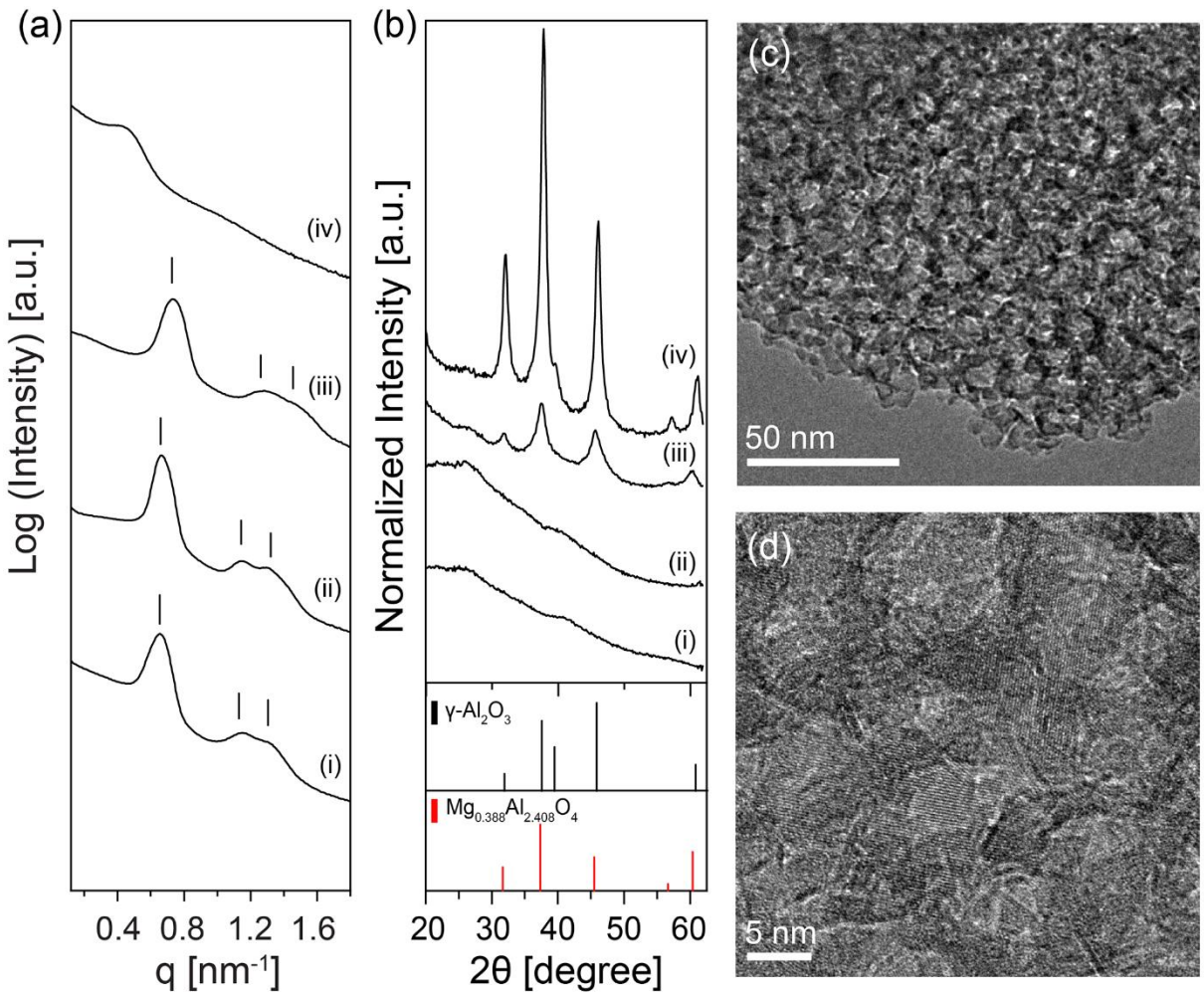

Figure S4. (a) SAXS and (b) WAXS patterns of mesoporous Al_2O_3-Mg-10 samples after conventional furnace annealing at (i) 600 °C, (ii) 700 °C, (iii) 800 °C, and (iv) 900 °C in air for 3 h. WAXS peak markings and relative intensities for γ-Al_2O_3 (black, PDF-00-010-0425), and $Mg_{0.388}Al_{2.408}O_4$ defect spinel (red, PDF-00-048-0528) are shown in (b). (c) TEM and (d) HR-TEM images of mesoporous Al_2O_3-Mg-10 samples after furnace calcination at 900 °C for 3 h exhibiting low structural order, attributed to the uncontrolled growth of the defect spinel crystallites.

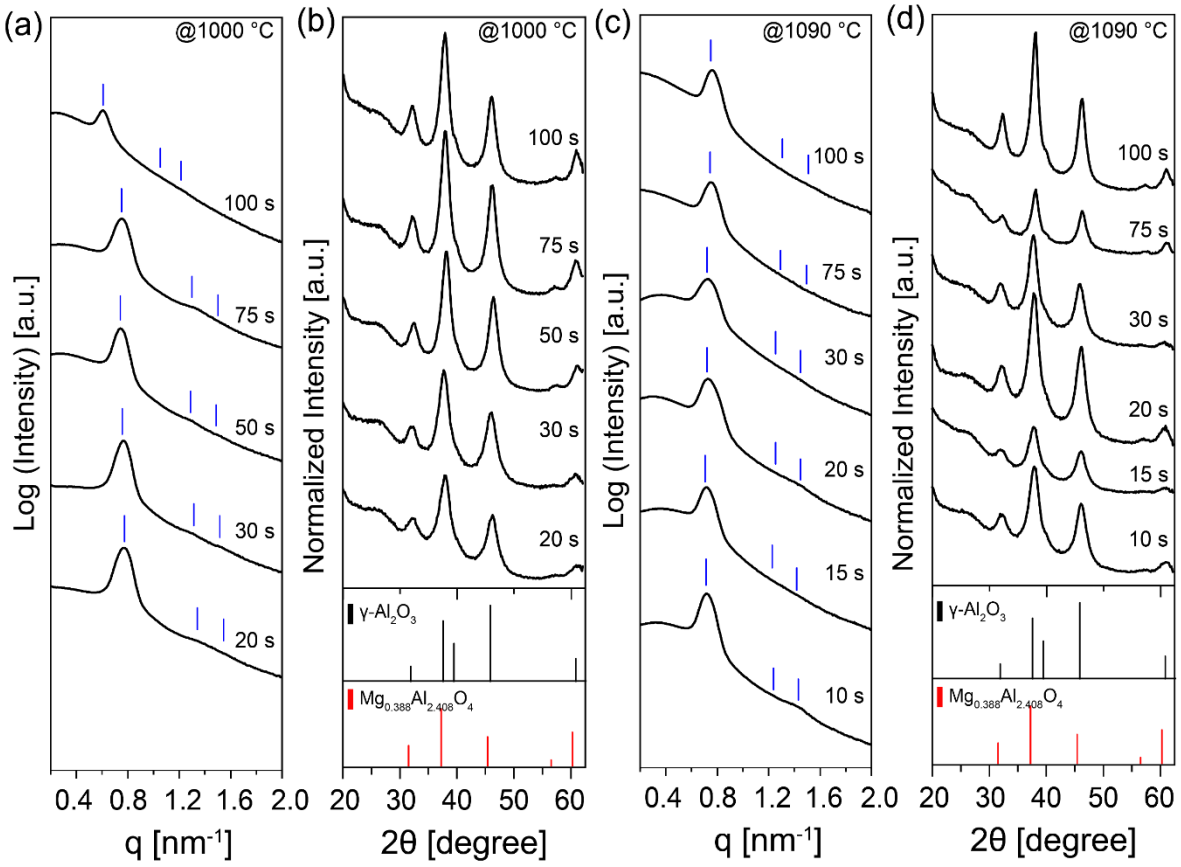

Figure S5. (a, c) SAXS and (b, d) WAXS patterns of mesoporous Al_2O_3-Mg-10 samples after Joule heating at 1000 °C (a, b) and 1090 °C (c, d) for various durations as indicated. Tick marks (blue) for the expected reflections of the *p6mm* symmetry are shown in (a, c). WAXS peak markings and relative intensities for γ-Al_2O_3 (black, PDF-00-010-0425) and $Mg_{0.388}Al_{2.408}O_4$ defect spinel (red, PDF-00-048-0528) are shown in (b, d).

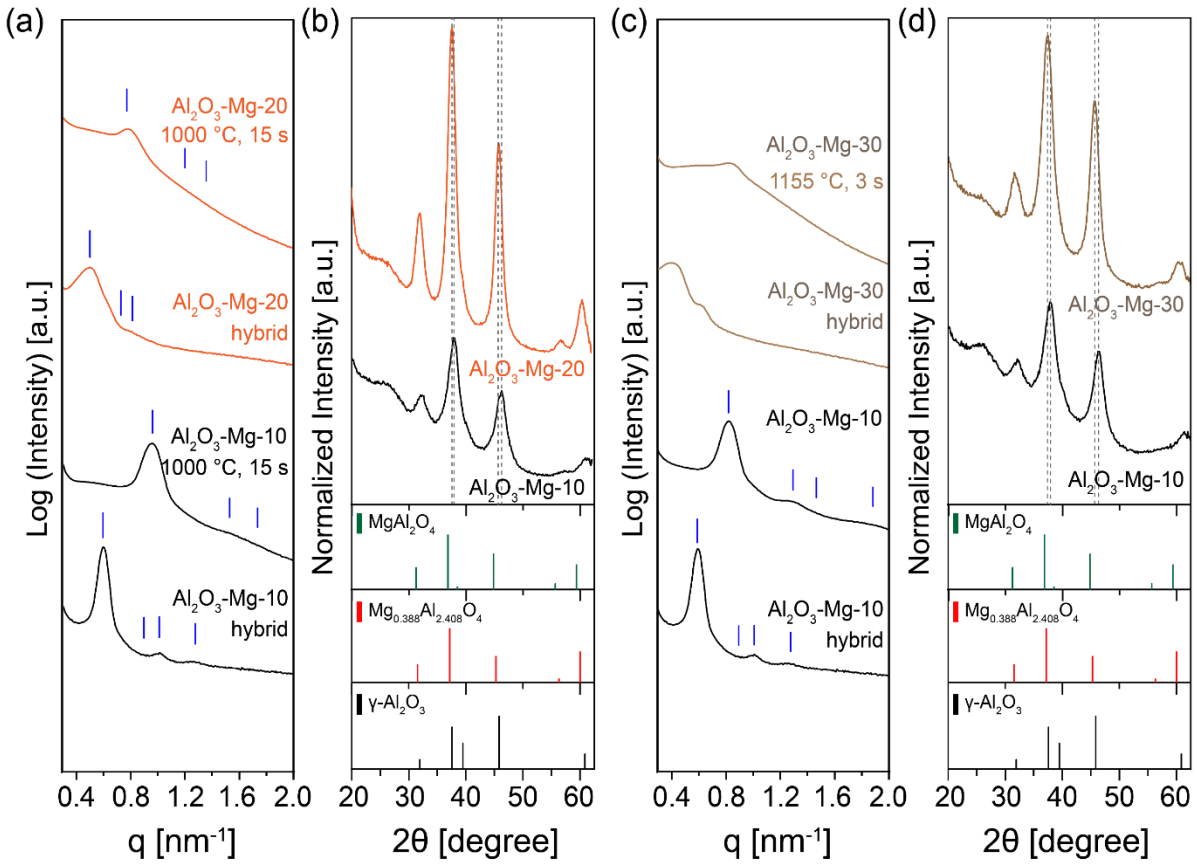

Figure S6. (a) SAXS and (b) WAXS patterns of Al_2O_3-Mg-10 and Al_2O_3-Mg-20 samples in the hybrid form and after Joule heating at 1000 °C for 15 s. (c) SAXS and (d) WAXS patterns of Al_2O_3-Mg-10 and Al_2O_3-Mg-30 samples in the hybrid form and after Joule heating at 1155 °C for 3 s. Tick marks (blue) for the expected reflections of the *p6mm* symmetry are shown in (a, c). WAXS peak markings and relative intensities for γ-Al_2O_3 (black, PDF-00-010-0425), $Mg_{0.388}Al_{2.408}O_4$ defect spinel (red, PDF-00-048-0528) and the stoichiometric $MgAl_2O_4$ spinel structure (green, PDF-00-048-0528) are shown in (b, d). The WAXS spectra of Al_2O_3-Mg-20 and Al_2O_3-Mg-30 after Joule heating match well with the spinel structure. Closer examination around 38° and 46° reveals that the principal peaks of samples with higher Mg content consistently appear to the left of those in the Al_2O_3-Mg-10 sample. This shift suggests that incorporating additional Mg atoms into their lattices has effectively expanded their lattice constants.

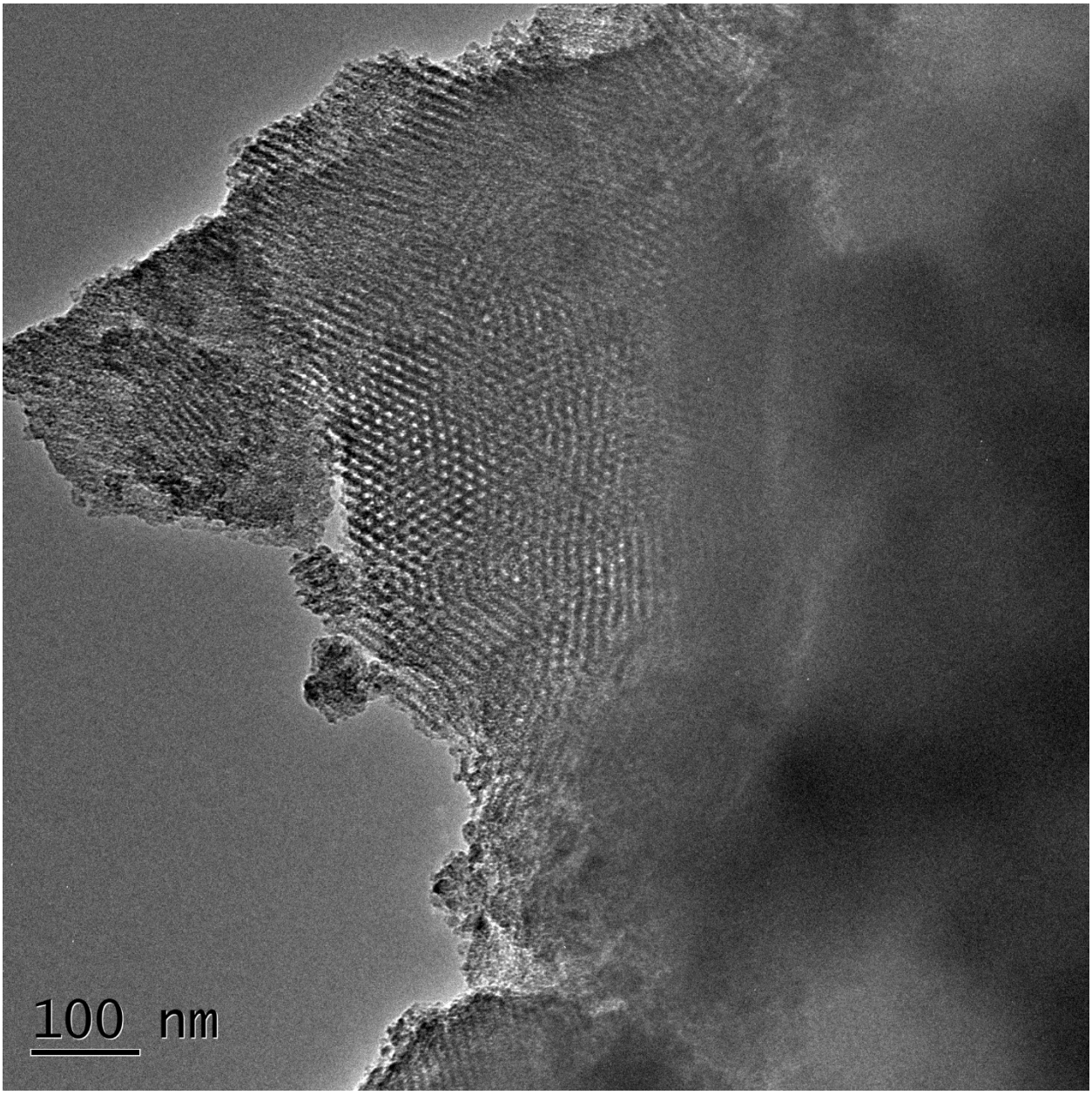

Figure S7. Lower magnification TEM image of mesoporous Al_2O_3-Mg-10 after Joule heating at 1155 °C for 3 s.

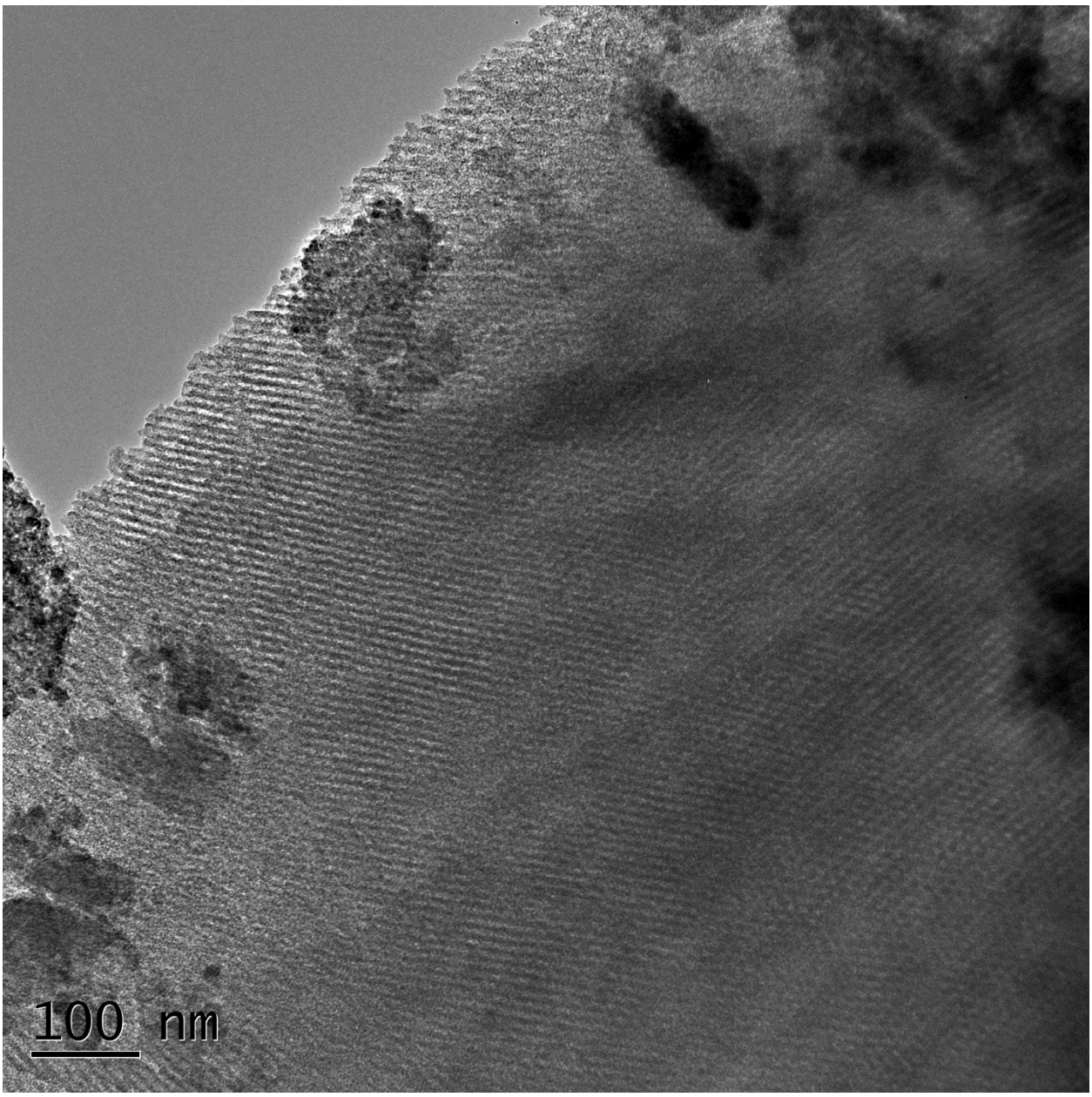

Figure S8. Lower magnification TEM image of mesoporous Al_2O_3-Mg-10 after Joule heating at 1155 °C for 3 s.

Table S1. SAED data analysis of Al_2O_3-Mg-10 after Joule heating at 1155 °C for 3 s was compared to ICCD $MgAl_2O_4$ dataset (PDF 00-021-1152). The presence of the (422) spinel plane, which is not easily identifiable in the γ-Al_2O_3 crystal structure, further supports the formation of the $Mg_xAl_yO_4$ defect spinel structure. .

Crystal Plane	Integrated Intensity Curve Peak Positions (1/r, nm^{-1})	*d*-spacing (Å)	ICCD $MgAlO_4$ *d*-spacing (Å) (PDF 00-021-1152)
(220)	3.46	2.89	2.8580
(311)	4.07	2.46	2.4370
(400)	4.91	2.04	2.0200
(422)	6.05	1.65	1.6500
(511)	6.37	1.57	1.5554
(440)	6.93	1.44	1.4289

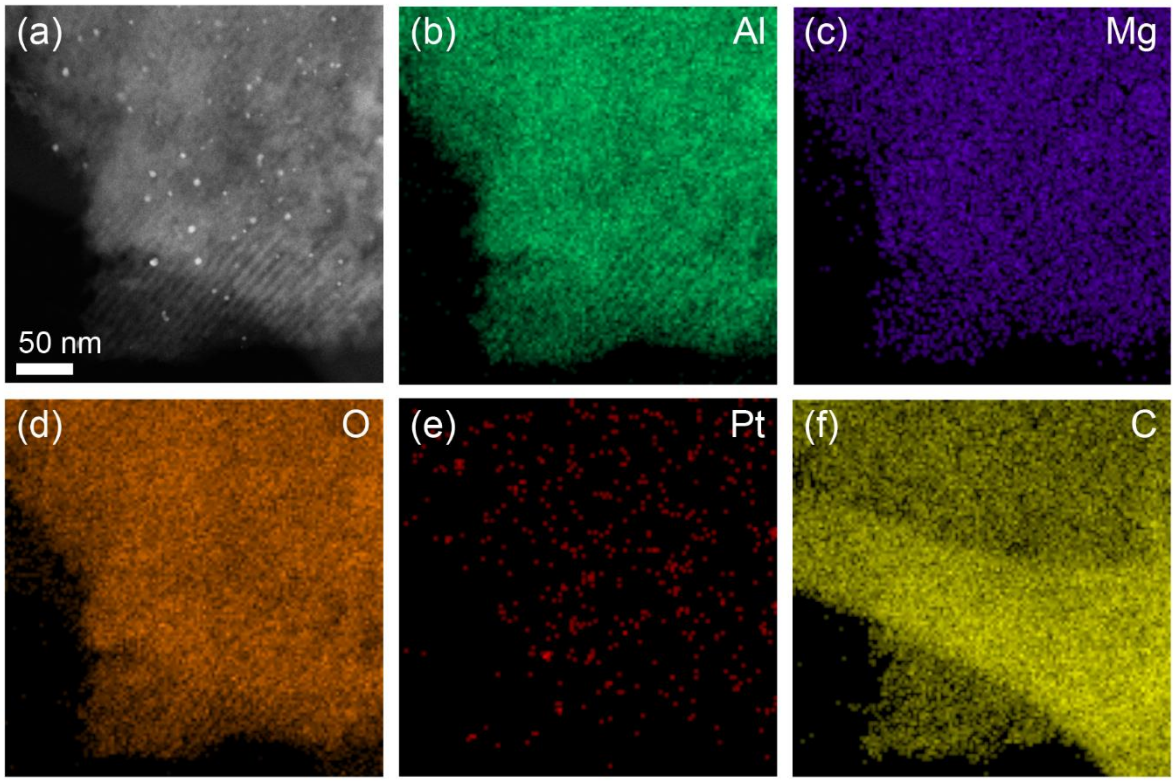

(g)

Element	Atomic %
Al	32.19
Mg	3.21
O	64.55
Pt	0.05

Figure S9. HAADF-STEM EDS elemental mapping analysis of ordered mesoporous 1wt%-Pt@$Mg_xAl_yO_4$ structures after Joule heating at 1155 °C for 4 s, as indicated. The table in panel (g) provides an estimated atomic ratio of four elements: Al, Mg, O, and Pt, obtained from EDS.

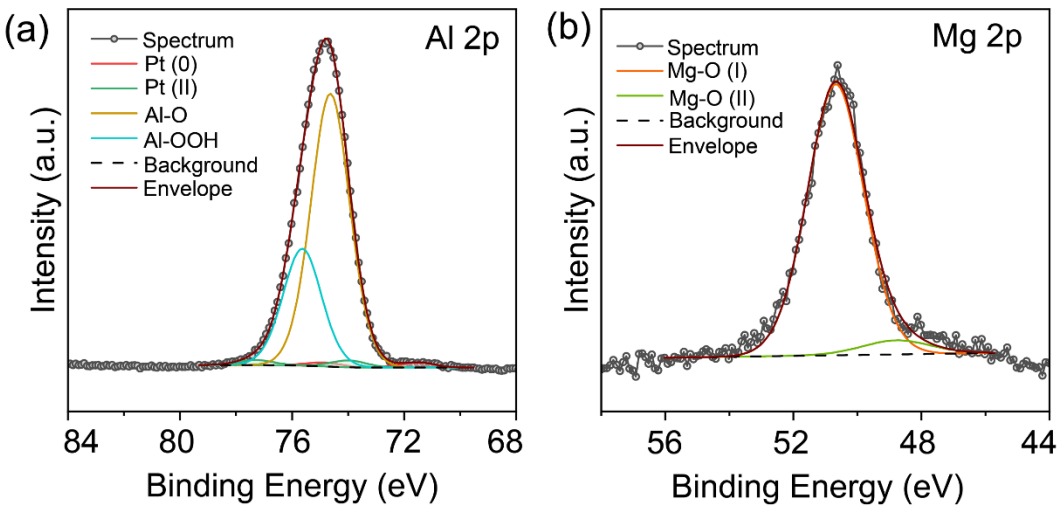

(c)

Element	Atomic %
Mg	10.5
Al	89.5

Figure S10. High-resolution XPS spectra of ordered mesoporous 1wt%-Pt@$Mg_xAl_yO_4$ structures after Joule heating at 1155 °C for 4 s, depicting the resolved component peaks in the (a) Mg 2p and (b) Al 2p regions. The table in panel (c) provides an estimated Mg/Al atomic ratio of close to 10:90., obtained from XPS. Due to the strong overlap between Al 2p and Pt 4f, we were not able to resolve the core levels of Pt within confidence limits, which is attributed to the low Pt content in the sample.

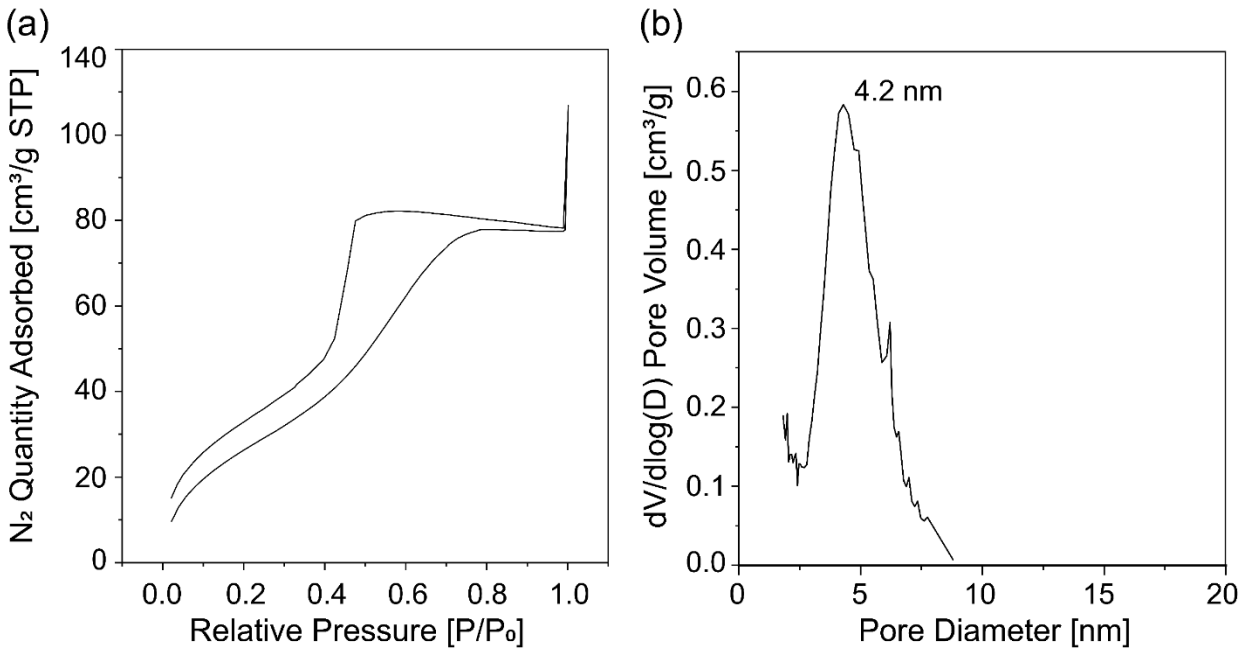

Figure S11. (a) Nitrogen sorption isotherm and (b) BJH pore size distribution of mesoporous Al_2O_3-Mg-10 after Joule heating at 1155 °C for 3 s.

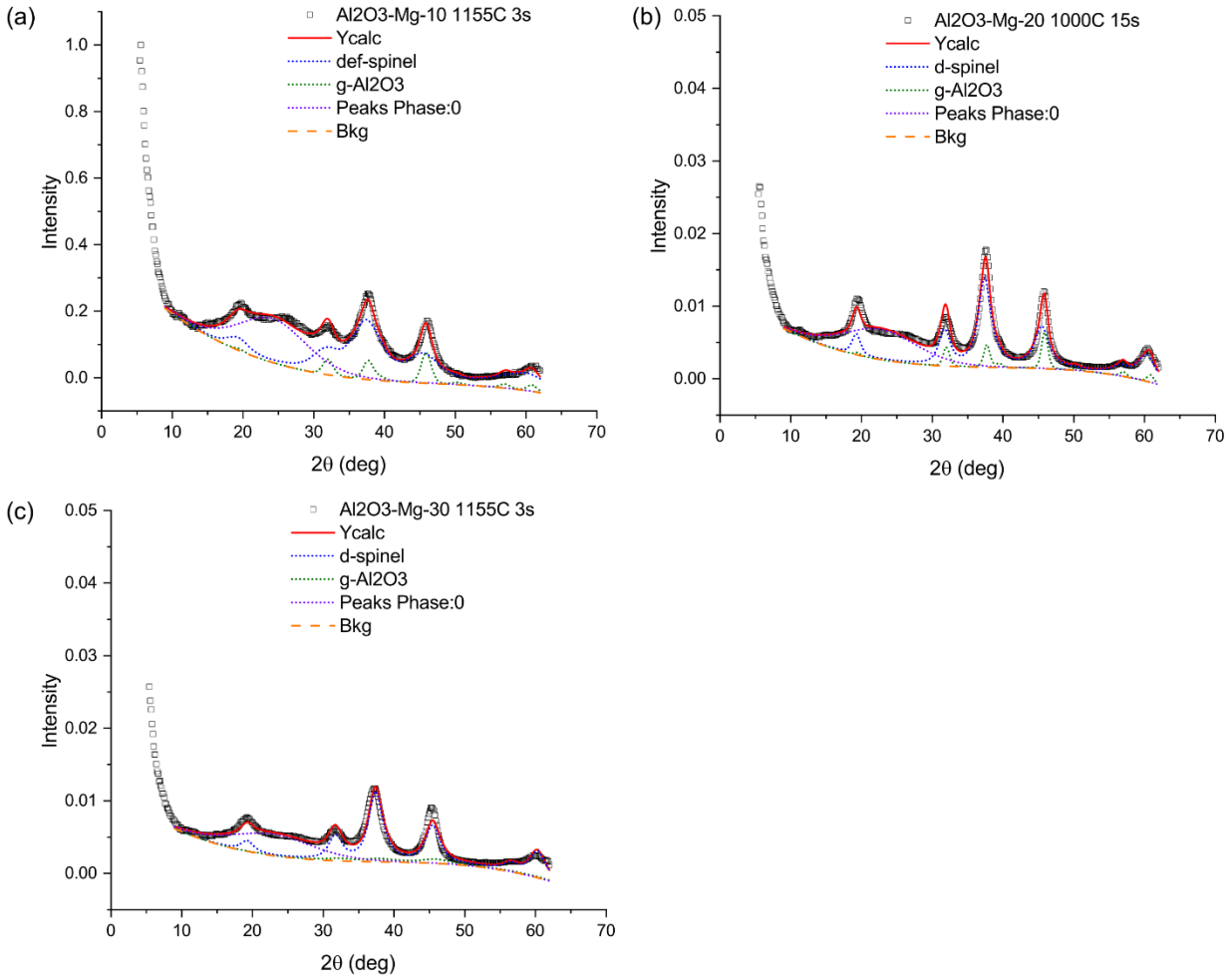

Figure S12. WAXS spectra of (a) Al_2O_3-Mg-10 sample after Joule heating at 1155 °C for 3 s, (b) Al_2O_3-Mg-20 Joule heating at 1000 °C for 15 s, (c) Al_2O_3-Mg-30 Joule heating at 1155 °C for 3 s, compared against simulated structures of $Mg_{0.388}Al_{2.408}O_4$ (*Z. Kristallogr. Cryst. Mater.* **1991**, *194* (1–4), 111–120.) and γ-Al_2O_3 (*Acta Crystallogr., Sect. B: Struct. Sci.* **1991**, *47* (5), 617–630.).

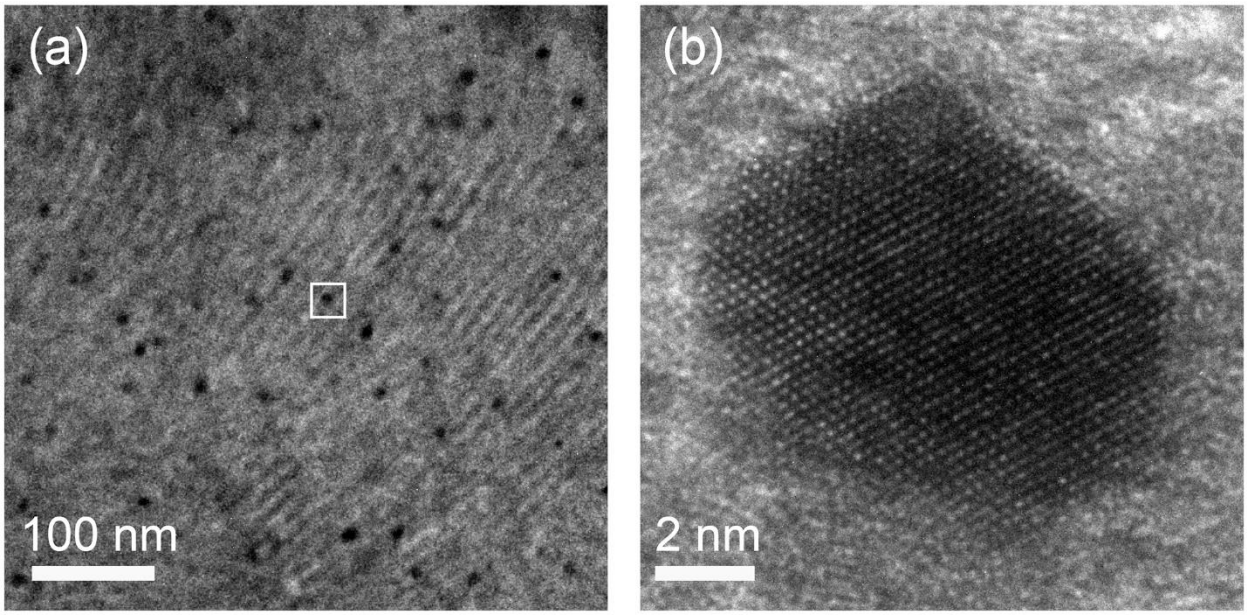

Figure S13. (a) TEM and (b) HR-TEM images of Pt nanoparticles uniformly dispersed on the walls of the 5wt%-Pt@$Mg_xAl_yO_4$ structures. The white box region in (a) denotes the Pt nanoparticle at a higher resolution in (d).

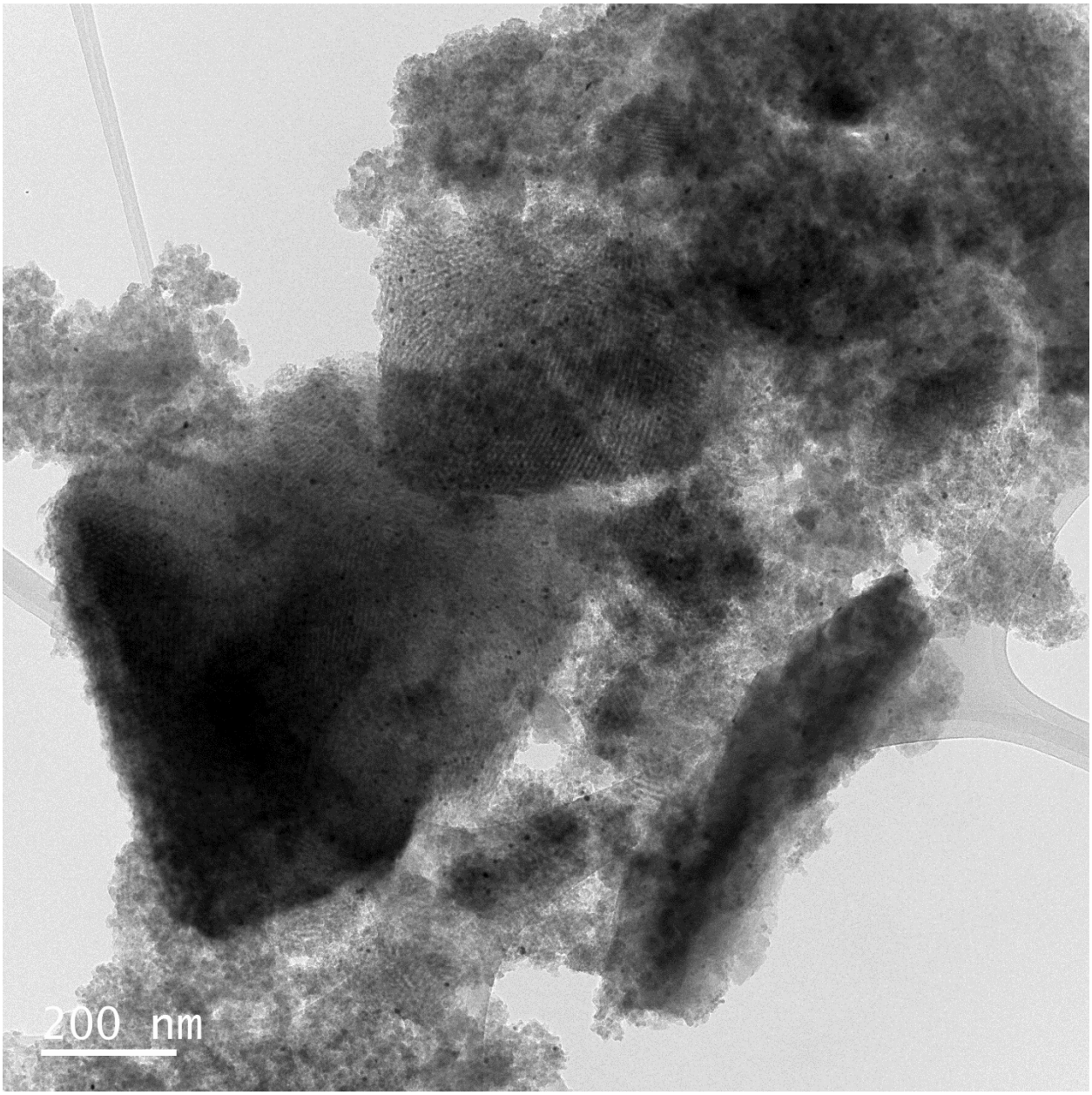

Figure S14. Lower magnification TEM image of 1wt%-Pt@$Mg_xAl_yO_4$ structures.

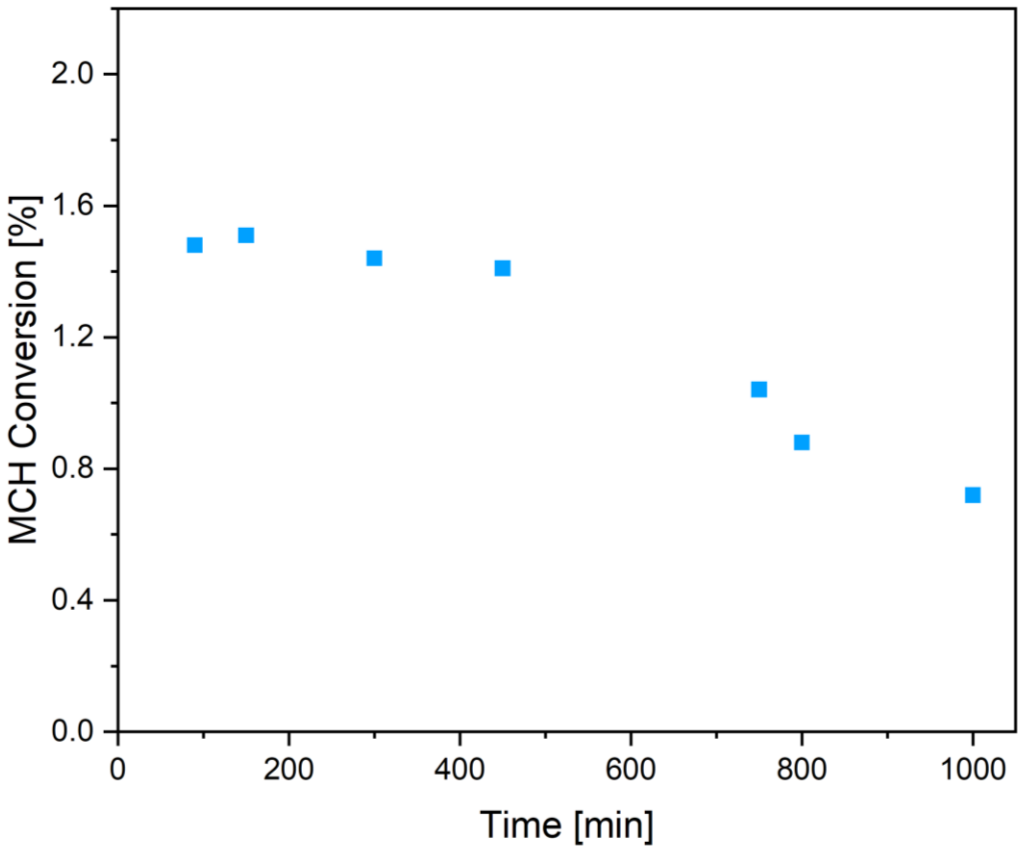

Figure S15. Methylcyclohexane conversion over 1wt%-Pt@$Mg_xAl_yO_4$ at 380 °C.

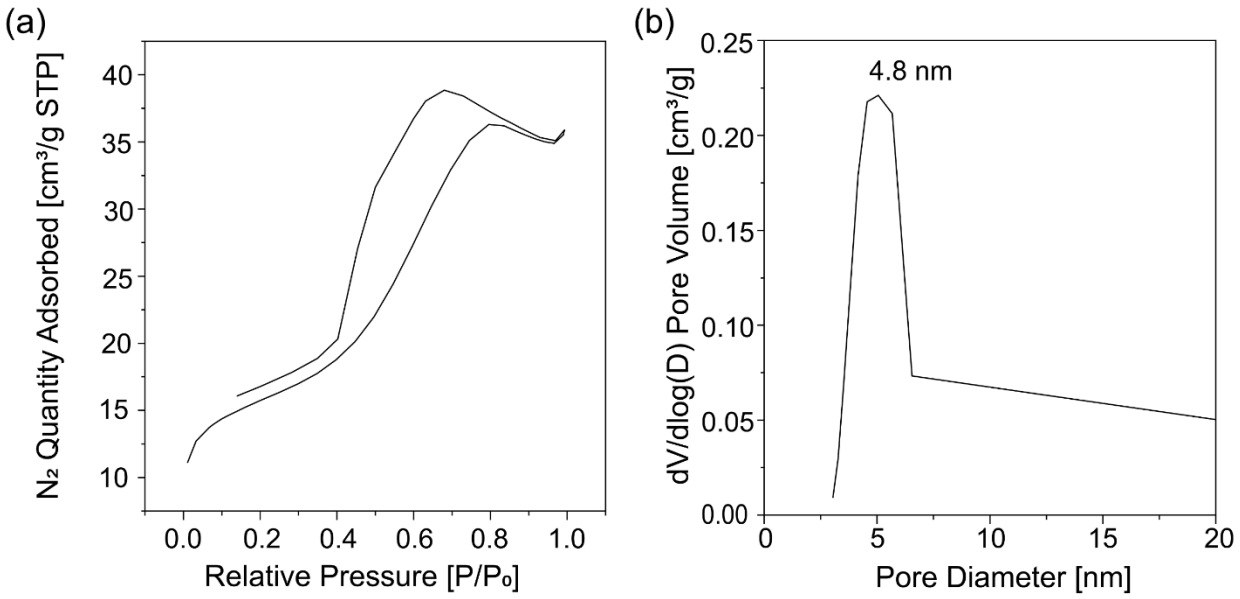

Figure S16. (a) Nitrogen sorption isotherm and (b) BJH pore size distribution of mesoporous 1wt%-Pt@$Mg_xAl_yO_4$.

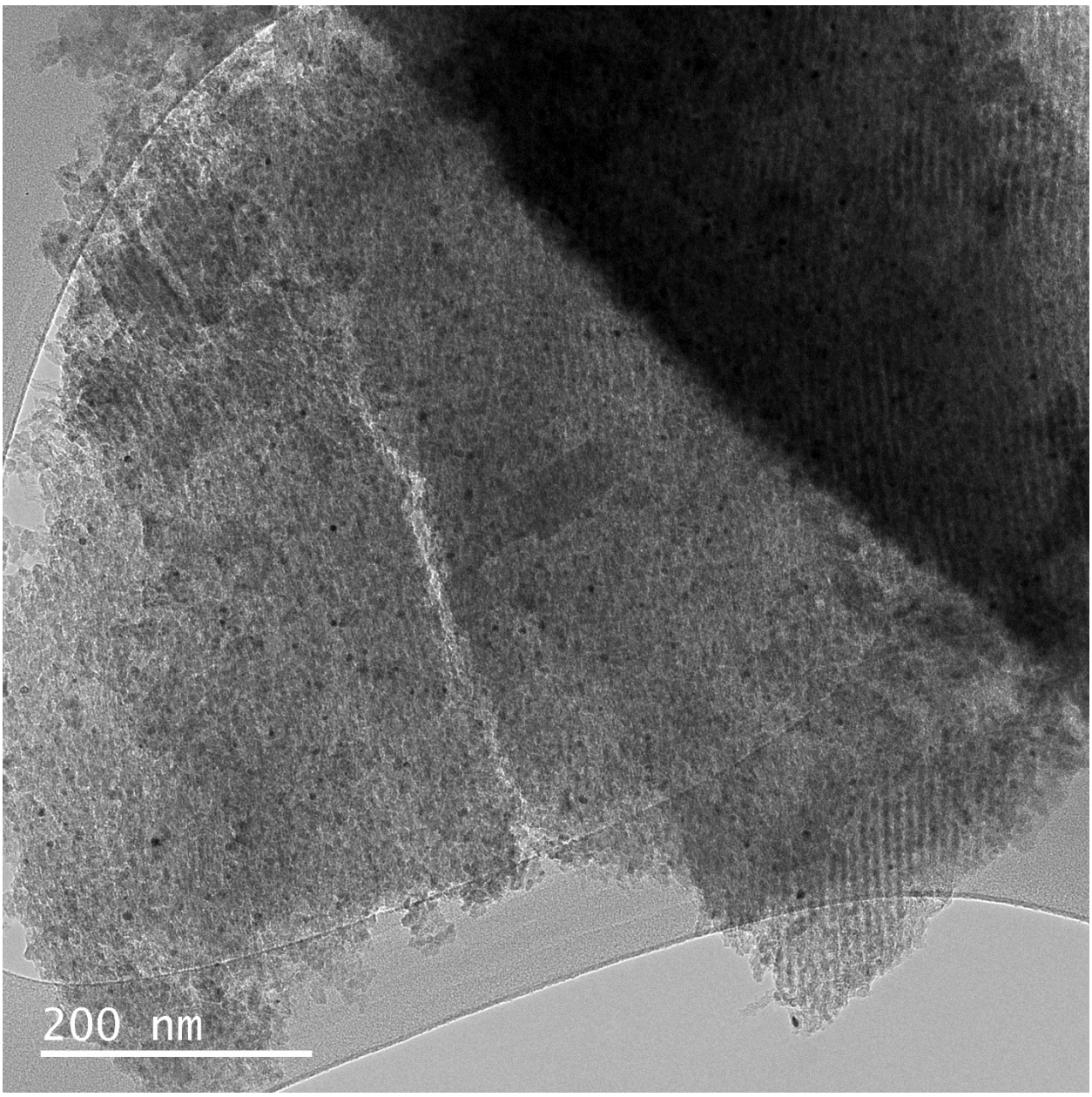

Figure S17. Lower magnification TEM image of 1wt%-Pt@$Mg_xAl_yO_4$ structures after methylcyclohexane dehydrogenation at 350 °C for 1000 min.